UNIVERSITY OF COPENHAGEN
NIELS BOHR INSTITUTE

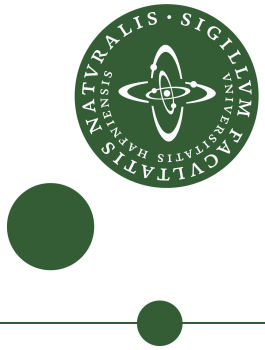

Master's Thesis

Semiconductor-Nanowire-Based Superconducting Qubits and Gate-Tunable Couplings

Author:
Thorvald W. Larsen

Supervisor:
Charles M. Marcus

August 16, 2016

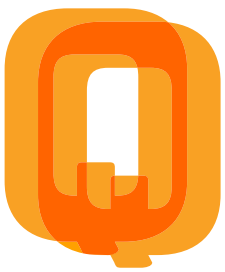

Center for
Quantum
Devices

Abstract

Superconducting transmon qubits are promising candidates for a scalable quantum processor. This thesis introduces a gatemon, a hybrid semiconductor-superconductor transmon qubit. An electrostatic gate controls the Josephson energy of a gatemon qubit by depleting the charge carriers in a semiconductor-based Josephson junction. We integrate a semiconductor nanowire with an epitaxially grown superconductor shell into a transmonlike circuit forming a gatemon. Strong coupling to a microwave cavity is observed as a vacuum-Rabi splitting. Full microwave control of single qubits together with a two-qubit interaction enabled by gate voltage pulses provide a universal gate set in gatemon qubits. Due to voltage control rather than flux control, dissipation in control lines is reduced. Furthermore, it is demonstrated that a switchlike, gate-tunable Josephson junction can modulate the resonance of a microwave cavity paving the way for gate tunable qubit-qubit couplings.

Acknowledgments

Firstly, I would like to thank my supervisor Charles Marcus. Thank you for giving me the opportunity to work in a state of the art physics laboratory with inspiring people. Thank you for teaching me that to do great physics you need to be bold and trust your intuition.

Next, I would like to thank my daily supervisor Karl Petersson. Thank you for taking me under your wing and teaching me everything about superconducting qubits, qubit manipulations, and high frequency measurements. It is a pleasure working in your team.

I would also like to thank Lucas Casparis and Anders Kringhøj for many fruitful discussions about physics and quantum information. Thank you for reminding me that physics is interesting even if experiments fails.

The experiment would not have happened if not for great advice/help in the cleanroom. Thank you Shiv Upadhyay for always being helpful and happy even when I call you at 10pm in the weekend.

Lastly, this time would not have been the same if not for all the great people in QDev so I would like to thank all of QDev for some memorable years!

Contents

List of Figures

Chapter 1

Introduction

Since the invention of the first solid state transistor in 1947 by John Bardeen, Walter Brittain, and William Shockley at Bell Laboratories it has come to shape the digital world. Transistors are the fundamental building blocks of the central processing unit (CPU) in a computer. Gordon E. Moore predicted in 1965 that the number of transistors per CPU would increase exponentially with time [1]. Surprising even to Moore himself the prediction still holds true. This has been achieved by rapidly decreasing the size of a transistor now approaching quantum mechanical limitations. Quantum tunneling, the phenomenon of a particle going through a barrier, sets a lower bound on the transistor size. However, there are interesting computational problems such as molecular simulation that even modern supercomputers cannot solve prompting the industry to search for new ways to increase CPU power.

One might think that the incredible growth in CPU power has been accompanied by some fundamental change of the computer. Surprisingly, modern computers are fully descibed by the first theoretical idea of a computer known as a Turing machine [2]. Theoretically a computer build from vacuum tubes can do the same computations as one built from transistors - only much slower. A fundamental change to the inner workings of a computer might increase computational power by more efficiently solving problems.

Quantum mechanics limits transistor size: is it possible to make a feature out of a bug? In the early 1980's R. Feynman and D. Deutsch pioneered the idea of a quantum computer [3, 4], where the bits of information are themselves quantum mechanical - known as quantum bits (qubits). A qubit is formed from a two-level system with states usually labeled $|0\rangle$ and $|1\rangle$. Qubits are still digital in the sense that they are either $|0\rangle$ or $|1\rangle$ when read out. However, they behave very differently during computation. Qubits can be in a superposition of the states $|\Psi\rangle = a_1|10\ldots0\rangle + a_2|01\ldots0\rangle + \cdots + a_{2^n}|11\ldots1\rangle$, where a_i are complex amplitudes and n is the number of qubits. A modest 300 qubit quantum computer can work with 2^{300} different states simultaneously - that is more states than there are atoms in the universe! The amplitudes of each state, a_i, can interfere during computation giving new possibilities for computation.

Even though the idea implies a new type of computation, it wasn't until 1994 that the field gathered interest. That year Peter W. Shor introduced a quantum algorithm

that efficiently factors integer numbers on a quantum computer [5]. It is easy for any computer to multiply two n-digit numbers. However, it is very hard to find prime factors of a large number on a classical computer.[1] It may seem weird that factoring is a hard problem, after all MATLAB has a function 'factor' that does it. However, the time it takes to find the prime factors of a number scales exponentially with the size of the number. The asymmetry in the complexity of multiplying compared to factoring lies at the heart of the modern encryption technique known as RSA encryption. For Shor's quantum algorithm the time it takes to factor only scales polynomially with the size of the number. This removes the asymmetry between multiplying and factoring.

The implications for modern encryption were enormous. Widely used encryption techniques rely on the fact that factoring is a *hard* problem. Shor effectively showed that breaking today's encryption is *easy* on a quantum computer. This ignited the field of quantum information and quantum computation. Other important problems, that are hard on classical computers but easy for quantum computers, are Grover's search algorithm and most notably Qauntum Simulations [6, 7].

1.1 Building a Quantum Computer

Realizing the potential for computations on a quantum computer the quest for a physical demonstration began. To guide the endeavor David P. DiVincenzo wrote a paper describing criteria for practical quantum computing [8]. The paper proposed five criteria for a quantum system to be a plausible host for a quantum computer.

- *Scalable qubit system:* The quantum system should have well-isolated, two-level systems making up the qubits. It should also be scalable in the number of qubits without degrading qubit performance.
- *Long coherence times:* The coherence time of the system should be much longer than the slowest gate.
- *Control:* A universal set of single- and two-qubit gates. A universal set means that any unitary qubit operation can by approximated to arbitrary precision by a finite number of gates from the set.
- *Readout:* High-fidelity, individual qubit readout.
- *Preparation:* A way to prepare the system in a known quantum state (e.g. $|00\ldots0\rangle$).

A quantum system is only useful as a quantum computer if it has *all* of these attributes. There is an inherent contradiction in these criteria that makes a quantum computer hard to build. Long lived qubits are created by isolating the system from the rest of the world. However, to control the qubits we necessarily need to interact with them and thereby break the isolation. It is easy to fulfill a couple of the criteria but very hard to fulfill them all simultaneously.

[1] This holds only for numbers with large prime factors.

Several approaches for quantum computing are actively being pursued: ion traps [9, 10], topological qubits [11, 12], and superconducting qubits [13–15] to name a few. A particularly promising candidate among superconducting qubits is the transmon qubit [16, 17]. The transmon qubit behaves as a weakly anharmonic LC-resonant circuit with the two lowest energy states forming the qubit two-level system. Since its conception almost a decade ago, the transmon has experienced rapid improvement in coherence times and scalability [18, 19].

No single qubit is expected to reach low enough error rates to do quantum computing without error correction (even classical computers implement error correction). Quantum error correction is challenging due to the no-cloning theorem. This means a qubit cannot simply be copied for redundancy as is possible with classical bits. The solution was found by P. W. Shor who came up with the first quantum error correcting code in 1995 [20]. The fundamental idea behind quantum error correction is to encode the quantum information in a non-local entangled state of many qubits. This is done in such a way that local errors are detectable without measuring the encoded quantum information which would collapse any superposition or entanglement of the encoded qubit. For further information on quantum error correction see [21, 22].

Recent results have demonstrated transmon qubits with one and two-qubit gate operation fidelities exceeding 99% [23] putting fault-tolerant quantum computing within reach [24]. Error correction has been demonstrated on single quantum states extending the lifetime of a multi-qubit state by increasing the number of qubits [25]. Furthermore 4-qubit correlation measurements have been performed [26], a crucial step toward practical quantum error correction.

At the heart of all superconducting qubits has been the $Al/Al_2O_3/Al$ Josephson junction. A Josephson junction is a weak link between two superconductors that forms a nonlinear inductor imbuing electrical circuits with the needed anharmonicity to isolate a two-level system. Usually two junctions are placed in parallel forming a superconducting quantum interference device (SQUID) that constitutes a flux tunable Josephson junction. An essential scaling problem for such superconducting qubits is the magnetic field needed for control. Single-qubit control is achieved by flowing $\sim$1 mA currents to induce local magnetic fields. As the number of qubits needed for useful quantum computing is estimated to be $>10^6$ [27] a current >1kA will need to flow from room temperature to cryogenic temperatures which seems almost as daunting as actually making that many qubits. This thesis reports a solution which exchanges dissipative currents with non-dissipative voltages by using a semiconductor-nanowire based Josephson junction [28, 29].

A quantum engineer has an additional design question: how are the qubits connected to each other? The most common connectivity scheme for transmons is a nearest neighbor coupling controlled by frequency tuning. When two transmons are detuned in frequency energy conservation effectively turns the coupling off. Even though this has demonstrated two-qubit gates close to fault-tolerant thresholds it is not an ideal method. When a single qubit is coupled to a few other qubits the crosstalk heavily complicates operations. This has lead to the development of new coupling schemes with individual

control [30–33]. This thesis presents results on implementing semiconductor-nanowire based Josephson junctions as superconducting switches controlling qubit couplings. Full control of qubit couplings would allow new quantum algorithms to take advantage of long distance couplings.

1.2 Outline of the Thesis

This thesis reports on the recent results from superconducting qubits based on an epitaxial InAs/Al core/shell nanowire Josephson junctions [34, 35]. The semiconductor introduces a field-effect tunability to a Josephson junction forming a novel element in superconducting circuits. Implementing it in a transmon circuit creates a voltage controlled superconducting qubit - a gatemon. Results on single and two qubits gatemons are presented showing that gatemons work similar to conventional transmons. These results have previously been published in T. W. Larsen *et al.* Phys. Rev. Lett. **115**, 127001 (2015) and L. Casparis *et al.* Phys. Rev. Lett. **116**, 150505 (2016) [29, 36]. Lastly, recent ideas of tunable qubit-qubit couplings implemented with nanowire Josephson junctions are presented alongside early results.

In Chapter 2 the fundamental theory of circuit quantum electrodynamics (cQED) and superconducting qubits will be introduced. A nanowire Josephson junction is also presented and some deviations from conventional junctions are considered. Fabrication and the measurement setup will be presented in Chapter 3. Chapter 4 presents results on single and two-qubit gatemon devices showcasing the gatemon as a qubit. Novel applications for nanowire Josephson junction to control qubit-qubit couplings are presented in Chapter 5.

Chapter 2

Theory

This chapter will present the theory of circuit quantum electrodynamics [37] and superconducting qubits loosely following notes by Steven M. Girvin [38]. It will start out with the simple LC circuit described in the flux basis. From there standard weak link Josephson junctions will be introduced to form a transmon circuit followed by the gatemon circuit with nanowire Josephson junctions. The rest of the chapter walks through single-qubit gates, readout, and two-qubit gates all components for quantum computing with transmons.

2.1 The LC Circuit

It is instructive to start with the simple LC circuit in Figure 2.1**A**. The usual way to solve the dynamics of the system is to take the charge on the capacitor as the coordinate. However, as it will become evident later, it is beneficial to consider the flux as our coordinate. The flux at a node, which is a connecting line between two circuit elements, is defined as the time integral of voltage at the node: $\phi(t) = \int_{-\infty}^{t} V(t')dt'$. In the LC circuit we have two nodes, the upper line and the lower line, and can freely chose one to be zero[1]. With one side set to zero we have $\dot{\phi} = V(t)$ where $V(t)$ is the voltage difference across the inductor. The voltage across an inductor we know: $V(t) = L\dot{I}(t) = \dot{\phi}(t)$, where I is the current through the inductor. By integration we find $\phi(t) = LI(t)$. The flux, $\phi(t)$, is simply the flux wound up in the inductor. With $\phi(t)$ as the coordinate we find the potential energy of the system as $U = \phi(t)^2/2L$ and similarly the kinetic energy is $T = \dot{\phi}(t)^2 C/2$. With the potential and kinetic energy one can write up the Lagrangian, $\mathcal{L} = T - U$, and with a Legendre transformation find the Hamiltonian as [38]

$$H = \frac{1}{2C}Q^2 + \frac{1}{2L}\phi^2, \tag{2.1}$$

where $Q = d\mathcal{L}/d\dot{\phi} = C\dot{\phi} = CV$ is the conjugate momentum which we recognize as the charge on the capacitor, hence the Q. As expected we find the Hamiltonian for a

[1] We can choose one side to have $V(t) = 0$ which will make $\phi(t) = 0$.

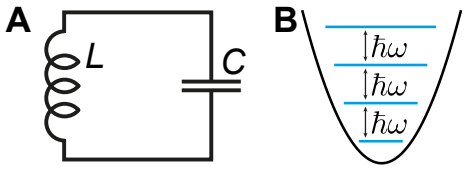

Figure 2.1: **A** An LC resonant circuit. **B** The energy spectrum of the quantized harmonic oscillator.

harmonic oscillator with resonance frequency $\omega = 1/\sqrt{LC}$.[2]

We can quantize the LC circuit by promoting the coordinate and its conjugate momentum to quantum operators obeying the canonical commutation relation

$$[\hat{\phi}, \widehat{Q}] = i\hbar. \tag{2.2}$$

The Hamiltonian for the harmonic oscillator can be transformed as usual

$$\widehat{H} = \frac{1}{2C}\widehat{Q}^2 + \frac{1}{2L}\hat{\phi}^2 = \hbar\omega\left(\hat{a}^\dagger\hat{a} + \frac{1}{2}\right), \tag{2.3}$$

where the creation and annihilation operators $\hat{a}^\dagger$ and $\hat{a}$ are given by

$$\begin{aligned}\hat{a} &= \frac{1}{\sqrt{2L\hbar\omega}}\hat{\phi} + i\frac{1}{\sqrt{2C\hbar\omega}}\widehat{Q}, \\ \hat{a}^\dagger &= \frac{1}{\sqrt{2L\hbar\omega}}\hat{\phi} - i\frac{1}{\sqrt{2C\hbar\omega}}\widehat{Q}.\end{aligned} \tag{2.4}$$

The energy spectrum of the harmonic oscillator is shown in Figure 2.1**B** with the well known equidistant energy levels. The eigenstates of the LC circuit are also called photon states where the state $|n\rangle$ has n photons in the resonator.

This energy spectrum has a crucial flaw if we want to make a qubit. We might identify the two lowest levels of the oscillator as $|0\rangle$ and $|1\rangle$ of a qubit. However, it is not possible to manipulate the qubit in these two states without exciting higher energy levels in the oscillator.[3] To make a qubit we need to have some anharmonicity in the system. Luckily nature has provided us with an anharmonic circuit element for the job: the Josephson junction.

2.2 Superconducting Qubits

Dissipative elements are naturally bad for qubit lifetimes. This leads us to exclusively work with superconductors in electrical circuits, which eliminates resistances in the wiring connecting circuit elements. Superconductivity originates from an electron-electron interaction that allow electrons to pair up in Cooper pairs described by a common macroscopic wave function ψ [39]. The magnitude of the wavefunction $|\psi|^2$ is equal to the density of

[2]The system is identical to a particle on a spring where the particle has coordinate $\phi(t)$, momentum Q, and mass C on the spring has spring constant $1/L$.

[3]It is possible to work around this problem by implementing nonlinearity in the control circuit. Recent results have shown active error correction in such systems [15].

Figure 2.2: Two superconducting electrodes (blue) sandwiching an insulator (grey) forms a Josephson junction. On the right the circuit symbol of a Josephson junction is shown.

Cooper pairs in the superconductor while the phase only manifests itself physically when coupling two superconductors.

The Josephson effect was theoretically predicted by B. D. Josephson in 1962 [40]. Josephson considered the case of a superconductor-insulator-superconductor (SIS) junction as shown in Figure 2.2. The Cooper pairs in each electrode can tunnel through the thin insulator allowing a current to flow through the insulator. Josephson made two predictions for such a weak link Josephson junction[4]

$$I_s = I_c \sin\varphi, \tag{2.5}$$

$$\frac{d\varphi}{dt} = \frac{2eV}{\hbar}, \tag{2.6}$$

where I_s is a dissipationless supercurrent tunneling through the insulator and φ is the difference in phase between the two wavefunctions ψ_i describing each superconductor. Equation (2.5) describes the dissipationless current flowing across the junction as a function of the phase difference φ. The parameter I_c is the critical current of the Josephson junction given by the maximal dissipationless current that can flow across the junction. If a larger current than I_c is forced through the junction it becomes resistive and a voltage difference develops. Equation (2.6) describes the time evolution of φ.

We can calculate the energy of a Josephson junction as a function of φ using the two equations

$$E = \int I_s V(t) dt = \frac{\hbar}{2e} \int I_s \frac{d\varphi}{dt} dt = \frac{\hbar I_c}{2e} \int \sin(\varphi) d\varphi = -\frac{\hbar I_c}{2e} \cos\varphi = -E_J \cos\varphi, \tag{2.7}$$

where $E_J = \hbar I_c / 2e$ is the Josephson energy.

Now consider the circuit of a Josephson junction in parallel with a capacitor and a nearby voltage source V_g as in Figure 2.3. We can describe the circuit with the phase difference across the junction and the number of Cooper pairs n on the island formed at the node connecting to the two capacitors and the Josephson junction. The Hamiltonian describing the system is

$$\widehat{H} = 4E_C(\hat{n} - n_g)^2 - E_J\widehat{\cos\varphi}, \tag{2.8}$$

where $E_C = e^2/2(C + C_g)$ is the charging energy of the island, $\hat{n}$ is the number operator for the number of Cooper pairs on the island, and $n_g = -C_g V_g / 2e$ is a charge offset. This is known as the Cooper pair box Hamiltonian. The voltage source V_g describes both the

[4]Weak link means that each Cooper pair has a low probability for tunneling through the insulator.

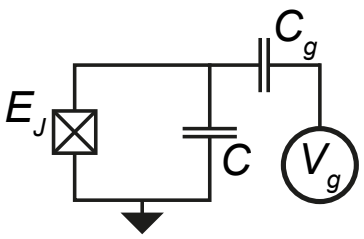

Figure 2.3: A Josephson junction in parallel with a capacitor and a voltage source coupled capacitively to the circuit.

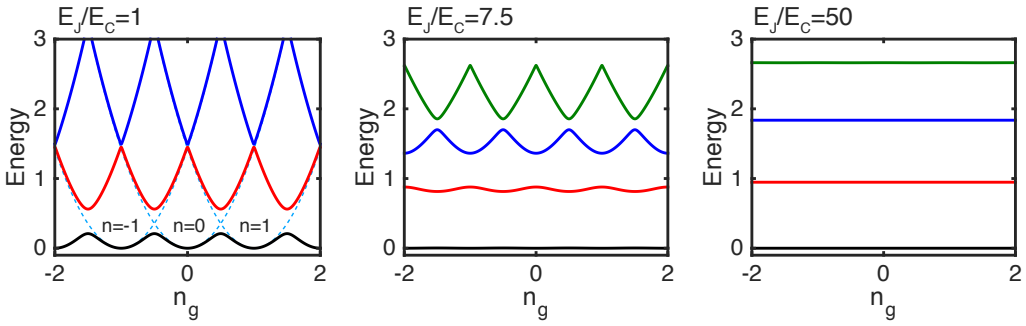

Figure 2.4: The lowest energy levels of the Hamiltonian in Equation (2.8) for different values of E_J/E_C. The energy of the Hamiltonian with $E_J = 0$ is plotted as light blue dotted parabolas in the first figure. In all figures the energy is normalized by $\sqrt{8E_C E_J}$. Figure inspired by [16].

coupling of a controlled charge offset and an uncontrolled environment.

The Cooper pair box Hamiltonian can be simulated numerically in the number basis with $\hat{n}|n\rangle = n|n\rangle$ and $\widehat{\cos\varphi} = \sum(|n\rangle\langle n+1| + |n+1\rangle\langle n|)$ [38]. In Figure 2.4 the energy levels are plotted as a function of the offset charge for different values of E_J/E_C. With $E_J = E_C$ we are in the Cooper pair box regime, where E_C dominates and charge is a good quantum number. The Josephson junction acts as a coupling term between charge states creating anticrossings. The energy spectrum is very anharmonic and isolating the two lowest energy levels to make a qubit is easy. However, any noise on the voltage source heavily influences the qubit energy leading to dephasing[5].

As E_J/E_C is increased we see the levels flatten out. Fluctuations in the voltage, or charge noise near the qubit, have almost no influence on the energy when $E_J \gg E_C$. This is the transmon regime. J. Koch et al. calculated that the charge dispersion flattens exponentially with E_J/E_C [16]. While charge noise can be suppressed exponentially the energy levels also seem to become equidistant as a harmonic oscillator.

To gain some intuition for the system in transmon regime we return to Equation (2.8). Earlier we defined a flux node from the voltage as $\phi = \int V(t)dt$. By integrating Equation (2.6) we find $\varphi = \int \frac{2e}{\hbar}V(t)dt$. It is tempting to conclude, mistakenly, that $\phi = \frac{\hbar}{2e}\varphi$. The superconducting phase difference φ is a periodic coordinate on the range $[-\pi, \pi]$ while ϕ can take any real value. However, let us assume that $|\varphi| \ll \pi$ so that $\phi \approx \frac{\hbar}{2e}\varphi = \frac{\Phi_0}{2\pi}\varphi$,

[5]Random changes in qubit energy induces random rotations around the Z axis of the Bloch sphere as we will see in Section 2.4.

where $\Phi_0 = h/2e$ is the superconducting flux quantum. Furthermore, in this limit we can Taylor expand the cosine term to second order (ignoring the offset charge n_g for the moment).

$$\begin{aligned}\widehat{H} &\approx 4E_C\hat{n}^2 - E_J\cos\left(2\pi\frac{\hat{\phi}}{\Phi_0}\right), \\ &\approx 4E_C\hat{n}^2 + E_J\left(\frac{2\pi}{\Phi_0}\right)^2\hat{\phi}^2, \\ &= \frac{1}{2C}\widehat{Q}^2 + \frac{1}{2L_J}\hat{\phi}^2\end{aligned} \tag{2.9}$$

where we have dropped a constant term and $L_J = (\hbar/2e)^2/E_J$ is inductance of the Josephson junction. This is simply the Hamiltonian for an LC circuit that we calculated earlier explaining why the energy levels became more equidistant. The resonance frequency of the system is $\omega = 1/\sqrt{CL_J} = \sqrt{8E_JE_C}/\hbar$.

Let us return to the assumption $|\varphi| \ll \pi$. Such an assumption can always be made classically but in quantum mechanics we have to check that it is consistent with quantum fluctuations. It is not possible to take the limit of small ϕ if the zero point fluctuations of ϕ are large. The mean square amplitude of the zero point fluctuations is

$$\phi_{ZPF}^2 = \langle 0|\hat{\phi}^2|0\rangle = \left(\frac{\Phi_0}{2\pi}\right)^2\left(\frac{2E_C}{E_J},\right)^{1/2}. \tag{2.10}$$

where $|0\rangle$ refers to the ground state of the Harmonic oscillator with creation and annihilation operators defined in (2.4). We find that in the transmon limit $E_J/E_C \gg 1$ the Taylor expansion is indeed valid.

Approximating the cosine potential with a harmonic potential gives us equidistant energy levels as in the LC circuit. To find the anharmonicity we can treat the fourth order term of the Taylor expansion as a perturbation

$$\begin{aligned}\widehat{H} &\approx \widehat{H}_0 + \widehat{V}, \\ \widehat{V} &= -\frac{E_J}{24}\left(\frac{2\pi}{\Phi_0}\right)^4\hat{\phi}^4,\end{aligned} \tag{2.11}$$

where $\widehat{H}_0$ is the harmonic Hamiltonian found in Equation (2.9). Using creation and annihilation operators for $\widehat{H}_0$ we can write $\hat{\phi}^4 = (\Phi_0/2\pi)^4(2E_C/E_J)\left(\hat{a}+\hat{a}^\dagger\right)^4$. Plugging into $\widehat{V}$ we have:

$$\widehat{V} = -\frac{1}{12}E_C\left(\hat{a}^\dagger+\hat{a}\right)^4 \approx -\frac{E_C}{2}\left(\hat{a}^\dagger\hat{a}^\dagger\hat{a}\hat{a} + 2\hat{a}^\dagger\hat{a}\right), \tag{2.12}$$

where we have dropped all terms with uneven numbers of annihilation and creation operators. We find a correction of E_C to the energy of the $|1\rangle$ state so that the qubit energy is $E_{01} = \sqrt{8E_JE_C} - E_C$. Crucially there is an extra correction to the energy of the $|2\rangle$ state giving a transition energy from the first excited state to the second of

Figure 2.5: Two superconducting electrodes (blue) sandwiching a semiconductor (green) form a Josephson junction. The semiconductor is tuned by a nearby gate electrode making the Josephson junction gate tunable. On the right the circuit symbol of a gate tunable Josephson junction is shown.

$E_{12} = \sqrt{8E_J E_C} - 2E_C$. The anharmonicity of the system can then be calculated as

$$\alpha = E_{12} - E_{01} \approx -E_C. \tag{2.13}$$

This anharmonicity allows us to isolate the first two states in the perturbed harmonic oscillator as our qubit states while being insensitive to charge noise. The fact that the charge dispersion is suppressed exponentially while the anharmonicity scales algebraically is responsible for the success of the transmon qubit.

2.3 Gatemons and Semiconductor Based Josephson Junctions

Above we described a transmon qubit made of a single Josephson junction in the weak coupling regime. The Josephson junction is usually realized by an $Al/Al_2O_3/Al$ sandwich with an aluminum oxide thickness of a few nanometers. When fabricated it has fixed characteristics allowing no direct control of the Josephson energy. To gain control of the effective Josephson energy one can place two junctions in parallel to form a SQUID which requires large currents to tune for typical geometries. A different approach has become possible as developments in semiconductor growth technology have produced new materials combining field effect tunability of semiconductors with superconductors.

A schematic of a superconductor-semiconductor-superconductor (SSmS) Josephson junction is shown in Figure 2.5. The carrier density of the semiconductor is tunable using a nearby gate which in turn tunes the critical current of the junction. By exchanging the SIS Josephson junction in the transmon circuit with an SSmS junction the transmon becomes gate tunable - a gatemon. The energy of the gatemon is tuned through the critical current $E_{01}(V_G) \propto \sqrt{E_J(V_G)} \propto \sqrt{I_c(V_G)}$.

Experiments have shown that it is possible to make high quality semiconductor nanowire proximitised by a superconductor [34, 35]. P. Krogstrup et al. have grown superconducting nanowires with a semiconducting InAs core and an epitaxial aluminum shell, see Figure 2.6**A**. The perfect crystalline interface between the semiconductor and superconductor makes these nanowires ideal for development of semiconductor based superconducting qubits.[6] A weak link in the superconducting nanowire is created by

[6] A weak coupling might create many quasiparticles in the superconductor which would be detrimental for superconducting qubits.

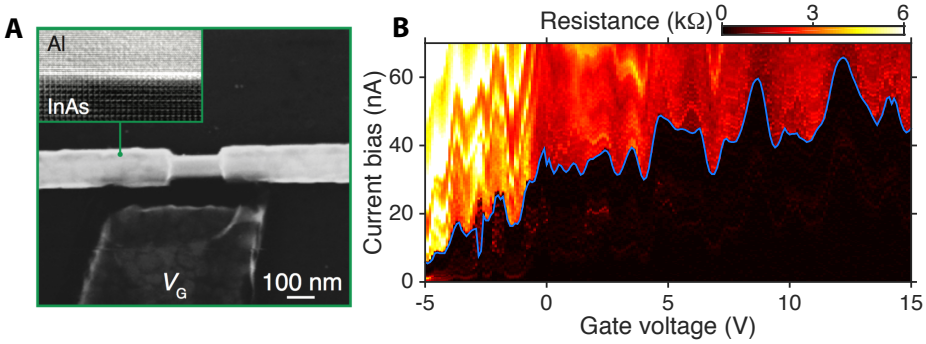

Figure 2.6: **A** The nanowire Josephson junction is formed by etching a small segment of the aluminum shell away. A nearby gate electrode tune the conductance of the semiconducting core. Inset shows the perfect crystalline interface between the InAs core and aluminum shell. **B** 4-probe resistance measurements of a nanowire based Josephson junction as a function of gate voltage and current bias. The critical current, I_c, of the junction is the lowest current value with non-zero resistance. The extracted critical current is indicated by a blue line.

chemically etching a small segment (∼180 nm) of the shell as shown in Figure 2.6**A**. The exposed semiconducting InAs core allows electric fields to tune the conductance of the core which influences the critical current of the junction. Placing a nearby gate electrode with voltage V_G induces a tunable electric field in the nanowire. Experimental measurements in Figure 2.6**B** reveal that the critical current is indeed gate tunable. The critical current is measured as the highest current that can be biased trough the junction without measuring a resistance. The critical current fluctuates aperiodically as a function of gate voltage with an upward trend. The electron mean free path of InAs nanowires has been found to be 150 nm [41]. As the junction length is longer than the mean free path, mesoscopic conductance fluctuations due to scattering across the junction show up as fluctuations in the critical current.

[7]The theory of a transmon shown in the previous section is based on the SIS junction. A gate-tunable superconducting qubit formed by a nanowire Josephson junction, a gatemon, will have different characteristics [42]. A nanowire based Josephson junction has a few highly transmitting channels in the semiconductor making the current-phase relation in Equation (2.5) inaccurate. It can be shown theoretically that the potential energy of such a junction is instead given by [43]:

$$E = -\sum_i K_i \sqrt{1 - \tau_i \sin^2(\varphi/2)}, \tag{2.14}$$

where τ_i is the transmission of the i'th channel K_i is proportional to the critical current of the i'th channel. To gain some intuition for the gatemon we can take the limit of $\tau_i = 1$ for all channels and let $4E_J = \sum K_i$. The factor 4 is a chosen such that the harmonic expansion of the cosine is of the same form as Equation (2.9). Then we can

[7]The rest of this section is heavily inspired by conversations with Michael Hell and Martin Leijnse.

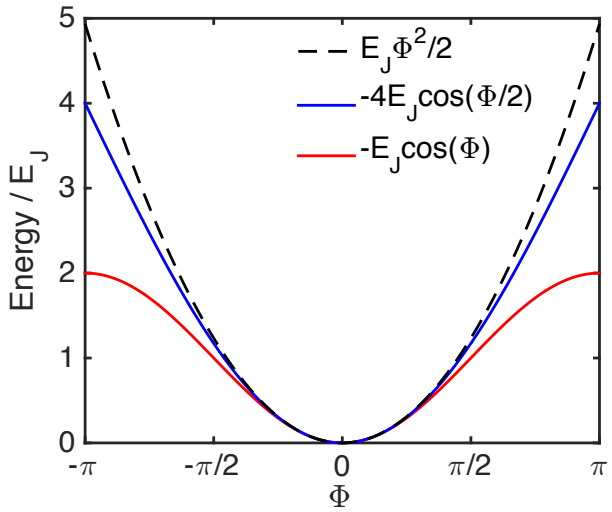

Figure 2.7: Josephson junction potentials for a tunnel junction, a junction with unity transmission, and the harmonic approximation in red, blue, and black respectively. The two cosine potentials are offset to match the harmonic potential at $\Phi = 0$.

write the energy as

$$E_{\tau_i=1} = -4E_J \cos(\varphi/2). \tag{2.15}$$

Notice a factor two difference in the cosine from the usual SIS junction energy ($E = -E_J \cos\varphi$). The Hamiltonian for a transmon with a Josephson junction with fully transmitting channels is:

$$\widehat{H}_{\tau_i=1} = 4E_C\hat{n}^2 - 4E_J\widehat{\cos(\varphi/2)}. \tag{2.16}$$

We can Taylor expand the Hamiltonian as before and find:

$$\begin{aligned} \widehat{H}_{\tau_i=1} &\approx \widehat{H}_0 + \widehat{V}_{\tau_i=1}, \\ \widehat{V}_{\tau_i=1} &= -\frac{4E_J}{24}\left(\frac{\pi}{\Phi_0}\right)^4 \hat{\phi}^4. \end{aligned} \tag{2.17}$$

The Harmonic part of the Hamiltonian is the same as in Equation (2.12) with a resonance frequency $\omega = \sqrt{8E_JE_C}/\hbar$. However there is a difference in the fourth order term as $\widehat{V}_{\tau_i=1} = \widehat{V}/4$. The factor four in the perturbation caries over to the anharmonicity which is $\alpha_{\tau_i=1} = -E_C/4$.

This intuitively makes sense if we plot the potentials of the Josephson junction together with the harmonic approximation as shown in Figure 2.7. Both potentials are well approximated by the same harmonic potential, hence the same $\widehat{H}_0$. However, it is clear that the potential for a fully transmitting junction more closely resembles the harmonic potential explaining the smaller anharmonicity. Measurements of the anharmonicity in gatemon qubits indicates that the nanowire Josephson junctions are in between the two limits [44].

2.4 Single qubit gates

Using a non-linear inductor in the form of a Josephson junction we are able to isolate the two lowest levels of the harmonic oscillator as our qubit state. With qubit states well defined we want to have coherent control of the state of the qubit.

In the previous section we saw that the transmon limit made the qubit insensitive to a voltage source coupled capacitively. However, these calculations assumed a time independent voltage source. Replacing the DC voltage supply with an AC and rewriting the Cooper pair box Hamiltonian[8] in Equation (2.8) we have

$$\widehat{H} = 4E_C\hat{n}^2 - E_J\widehat{\cos(\varphi)} + \frac{2eC_g}{C}V_g(t)\hat{n}. \tag{2.18}$$

We can write the applied AC voltage as $V_g(t) = v_R\cos(\omega t) + v_I\sin(\omega t)$ where v_R and v_I are the in phase and out of phase components of the voltage respectively. Writing the Hamiltonian in the transmon energy eigenstates, $|i\rangle$, with energies E_i gives

$$\begin{aligned}\widehat{H} &= 4E_C\hat{n}^2 - E_J\widehat{\cos(\varphi)} + 2e\beta[v_R\cos(\omega t) + v_I\sin(\omega t)]\hat{n} \\ &= \sum_i E_i|i\rangle\langle i| + \sum_{i,j} 2e\beta\langle i|\hat{n}|j\rangle\left[v_R\cos(\omega t) + v_I\sin(\omega t)\right]|j\rangle\langle i|,\end{aligned} \tag{2.19}$$

where $\beta = C_g/C$. The matrix elements $\langle i|\hat{n}|j\rangle$ were calculated by J. Koch et al. [16]. They found that in the transmon limit the only relevant contributions are couplings between states that differ by one excitation. Truncating the transmon energy space to a two-level system we are left with coupling between zero and one states.

$$\widehat{H} = \frac{\hbar\omega_{01}}{2}\hat{\sigma}_z + 2e\beta\langle 0|\hat{n}|1\rangle\left[v_R\cos(\omega t) + v_I\sin(\omega t)\right](\hat{\sigma}_+ + \hat{\sigma}_-), \tag{2.20}$$

where $\hat{\sigma}_i$ are the Pauli matrices, $\hbar\omega_{01} = E_1 - E_0$, and $\langle 0|\hat{n}|1\rangle = \langle 1|\hat{n}|0\rangle$. In a rotating frame of the drive and invoking the rotating wave approximation the Hamiltonian reduces to

$$\begin{aligned}\widehat{H}_R &= e^{i\omega t\hat{\sigma}_z/2}\widehat{H}e^{-i\omega t\hat{\sigma}_z/2} - \frac{\hbar\omega}{2}\hat{\sigma}_z \\ &= \frac{\hbar(\omega_{01}-\omega)}{2}\hat{\sigma}_z + \frac{\hbar}{2}[\Omega_R\hat{\sigma}_x - \Omega_I\hat{\sigma}_y],\end{aligned} \tag{2.21}$$

where $\Omega_j = \frac{2e}{\hbar}\beta\langle 0|\hat{n}|1\rangle v_j$ is the Rabi frequency. A classical voltage signal $V(t)$ on an electrode capacitively coupled to the qubit can drive the qubit from $|0\rangle$ to $|1\rangle$ and back with a frequency given by Ω_j. By tuning the phase of the signal we can drive the qubit around an arbitrary axis in the XY plane of the Bloch sphere allowing us to perform any unitary operation on the qubit. Furthermore, a change in qubit energy $\hbar\omega_{01}(V_{\mathrm{G}})$ will induce rotations around the Z axis. It is therefore critical to have a stable qubit energy.

We have shown that we can couple to the qubit capacitively with AC voltage pulses.

[8] For these calculations we are ignoring the fact that the gatemon has a modified junction potential. The difference would show up in the calculation of the matrix elements $\langle i|\hat{n}|j\rangle$ which is beyond the scope of this thesis.

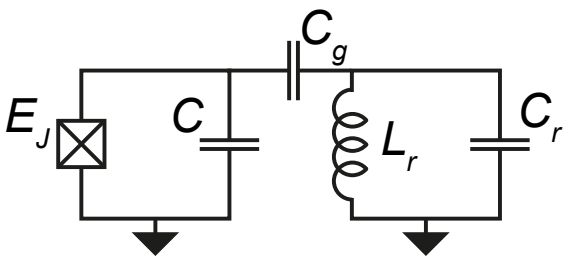

Figure 2.8: A transmon circuit coupled capacitively to a harmonic LC circuit.

On the other hand this also means the qubit can be driven by the environment. The decay rate, $\gamma = 1/T_1$, due to the drive electrode is given by: $\gamma = \left(\frac{2e}{\hbar}\beta\langle 0|\hat{n}|1\rangle\right)^2 S(\omega_{01})$, where $S(\omega_{01})$ is the noise spectral density at the qubit frequency [45]. One has to be careful not to compromise the lifetime of the qubit when coupling it to drive electrodes[9]. Fortunately C_g/C is very small in these systems and effective filtering of the drive lines at the qubit frequency lowers the noise spectral density.

2.5 Readout

For transmons and many other types of superconducting qubits one can readout the qubit state by probing the frequency of a coupled harmonic oscillator. Such a system, a qubit coupled to a single resonant mode in electrical circuits, is described by cQED [37]. The qubit and resonator can be coupled capacitively as shown in Figure 2.8. If we assume a two-level system for the transmon we can write the full Hamiltonian of the system as:

$$\widehat{H} = \hbar\omega_r \hat{a}^\dagger \hat{a} + \hbar\frac{\omega_q}{2}\hat{\sigma}_z + \frac{2eC_g}{CC_r}\widehat{Q}_r\hat{n}, \tag{2.22}$$

where $\widehat{Q}_r$ is the charge operator of the LC circuit. The two first terms describes the isolated resonator and qubit systems respectively. The last terms is the coupling term. The coupling term is of the same form for the driven Hamiltonian in Equation (2.18). Only now the voltage that the qubit sees is given by voltage on the resonator $V_r = Q_r/C_r$ instead of an applied voltage on an electrode.

Focusing only on the coupling term of the Hamiltonian we rewrite it as raising and lowering operators for each system.[10]

$$\widehat{H}_{qr} = \frac{2eC_g}{C}\langle 1|\hat{n}|0\rangle V_{\mathrm{ZPF}}(\hat{a} + \hat{a}^\dagger)(\hat{\sigma}_+ + \hat{\sigma}_-), \tag{2.23}$$

where $V_{\mathrm{ZPF}} = Q_{\mathrm{ZPF}}/C_r = \sqrt{\hbar\omega_r/2C_r}$ is the zero point fluctuation of the voltage across the capacitor C_r. Defining the coupling constant $\hbar g = \frac{2eC_g}{C}\langle 1|\hat{n}|0\rangle V_{\mathrm{ZPF}}$ and making the

[9] The same decay process is present for the gate controlling the Josephson junction.

[10] We have changed the phase of the resonators raising and lowering operators $\hat{a}$ and $\hat{a}^\dagger$ as is conventional for these equations in the field [38].

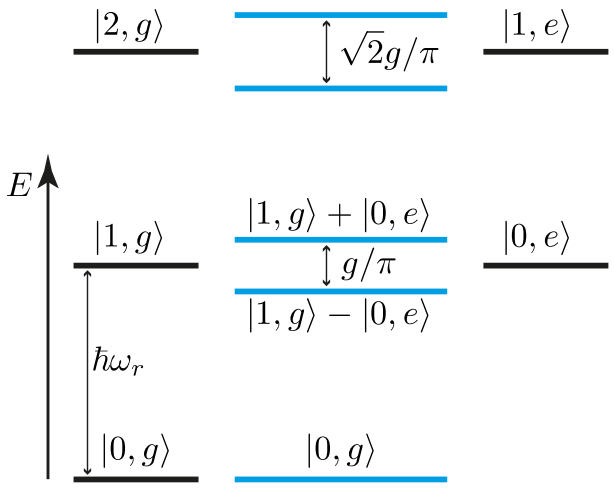

Figure 2.9: The energy spectrum of the Jaynes-Cumming Hamiltonian in the resonant regime with $\omega_r = \omega_q$. Left are the states $|n,g\rangle$ where n is the number of photons in the resonator and $|g\rangle$ is the ground state of the qubit. Adding a photon to the resonator states increases the energy by $\hbar\omega_r$. Right are states $|n,e\rangle$ where $|e\rangle$ is the excited state of the qubit raising the energy by $\hbar\omega_q$. In blue are the eigenstates of the coupled system described by Equation (2.25).

rotating wave approximation the coupling Hamiltonian simplifies to

$$\widehat{H}_{qr} = \hbar g(\hat{a}\hat{\sigma}_+ + \hat{a}^\dagger\hat{\sigma}_-). \tag{2.24}$$

Returning to the full Hamiltonian of both systems we find the Jaynes-Cumming Hamiltonian

$$\widehat{H} = \hbar\omega_r\hat{a}^\dagger\hat{a} + \hbar\frac{\omega_q}{2}\hat{\sigma}_z + \hbar g(\hat{a}\hat{\sigma}_+ + \hat{a}^\dagger\hat{\sigma}_-). \tag{2.25}$$

There are two distinct regimes for the Jaynes-Cumming Hamiltonian. The resonant regime when $\omega_r = \omega_q$ and the dispersive regime with $|\omega_q - \omega_r| \gg g$. In the resonant regime the qubit and resonator states hybridize as shown in Figure 2.9. In the one excitation manifold the resonator-qubit states are a mixture of a photon in the resonator and an excitation in the qubit. The splitting is known as the vacuum-Rabi splitting as a qubit excitation does Rabi oscillations with the vacuum state of the resonator. To observe the splitting we need g/π to be larger than the linewidth of both the qubit and resonator. This regime cannot be used for qubit operation but demonstrates strong qubit-resonator coupling.

For qubit operation we want to be in the dispersive regime. This regime allows us to simplify the Jaynes-Cumming Hamiltonian in Equation (2.25) by expanding in the small parameter g/Δ, where $\Delta = \omega_q - \omega_r$ is the detuning. One has to be careful when doing the expansion as higher energy levels of the transmon are important. Therefore the expansion is done on the full multilevel system and then truncated to a two level system afterwards [16]. The calculations are long and tedious and we will refrain from

going through them here. The resulting Hamiltonian is

$$\widehat{H} = \hbar\left(\omega_r - \frac{\chi_{12}}{2}\right)\hat{a}^\dagger\hat{a} + \hbar\frac{1}{2}(\omega_q + \chi_{01})\hat{\sigma}_z + \hbar\chi\hat{a}^\dagger\hat{a}\hat{\sigma}_z, \tag{2.26}$$

where $\chi_{ij} = g_{ij}/(\omega_{ij} - \omega_r)$ and $\chi = \chi_{01} - \chi_{12}/2$.[11] The coupling strength is given by $g_{ij} = \frac{2eC_g}{\hbar C}\langle i|\hat{n}|j\rangle V_{\mathrm{ZPF}}$.

There are three terms in the Hamiltonian coming from the coupling. The first two terms are called *Lamb shifts* giving a correction to the qubit and resonator frequencies. The last term can be interpreted in two ways. We can view it as a correction to the qubit frequency dependent on the number of photons in the resonator. This is known as the Stark shift of the qubit and can be exploited to measure photon number states in the resonator [46, 47]. Equally valid we can interpret the term as a qubit dependent dispersive shift of the resonator

$$H = \hbar\left(\omega_r' + \chi\sigma_z\right)a^\dagger a + \hbar\frac{1}{2}\omega_q'\sigma_z, \tag{2.27}$$

where $\omega_q' = \omega_q + \chi_{01}$ and $\omega_r' = \omega_r - \chi_{12}$. Written in this form we explicitly see the qubit state dependence of resonance frequency of the resonator. The dispersive shift can be approximated in the transmon limit to $\chi = \alpha g^2/\Delta^2$ where α is the anharmonicity of the qubit. By probing the frequency of the resonator with a classical microwave tone we can infer the qubit state. Furthermore, this is a so called quantum non-demolition (QND) readout scheme which means that the qubit is left in the measured state after readout [37]. This can be exploited to perform qubit state preparation with fast feedback [48].

As for the single-qubit gates we have to be careful not to compromise qubit performance when coupling components to the qubit. In the dispersive regime a qubit can decay via the resonator through an effect known as the Purcell effect. If a resonator has a photon decay rate κ then the Purcell effect dictates a qubit decay rate $\gamma_\kappa = (g/\Delta)^2\kappa$ [49]. The decay rate of the resonator also controls the speed at which we can measure its frequency. For realistic values it is possible to have long lifetimes while still having reasonable fast readout: $\gamma_\kappa = (100\text{ MHz}/2\text{ GHz})^2(1/200\text{ns}) = 1/80\ \mu\text{s}$. By implementing a Purcell filter the effect can be greatly reduced allowing for much faster readout [50].

2.6 Multiqubit Coupling

The last thing we need to theoretically fulfill the DiVincenzo criteria is a universal gate set. We can do any single-qubit gate but to have a universal gate set we need a multi-qubit gate. For transmons the most widely used multi-qubit gate is a two-qubit controlled phase gate (c-phase gate). However, before we look at the specific gate we need to engineer a coherent two-qubit interaction.

There are a multiple ways to setup qubit-qubit interactions for transmons. Here we will go through the theory for two most used types of qubit-qubit couplings. Both

[11] If the system is truncated before the approximation all the terms with χ_{12} does not show up as the $|2\rangle$ state is not present.

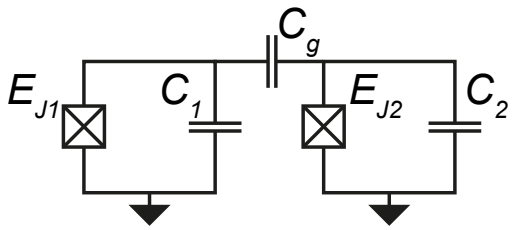

Figure 2.10: Two transmon qubits coupled capacitively.

methods rely on coupling the charge degree of freedom in the transmons. One is a direct capacitive coupling that is very similar to the qubit resonator coupling [51] while the other is a coupling mediated by a resonator [52].

Two transmons can be coupled as shown schematically in Figure 2.10. The Hamiltonian describing the system is

$$\widehat{H} = \hbar\frac{\omega_1}{2}\hat{\sigma}_{z,1} + \hbar\frac{\omega_2}{2}\hat{\sigma}_{z,1} + \hbar J(\hat{\sigma}_{-,1}\hat{\sigma}_{+,2} + \hat{\sigma}_{+,1}\hat{\sigma}_{-,2}), \tag{2.28}$$

where $J = \frac{(2e)^2 C_g}{C_1 C_2}\langle 0|_1\hat{n}_1|1\rangle_1\langle 1|_2\hat{n}_2|0\rangle_2$ is the coupling strength. This is the Jaynes-Cumming Hamiltonian with the resonator replaced by a qubit. In the transmon limit we can write the coupling term as $J = \frac{C_g\sqrt{\omega_1\omega_2}}{2\sqrt{C_1 C_2}}$. If the qubits are far detuned in frequency the coupling term becomes negligible due to energy conservation. By pulsing the qubits into resonance in a controlled manner, for instance by changing the gate voltage on a nanowire Josephson junction, one can turn on the coupling for a short time to perform a gate.

A somewhat more involved system is the qubit-resonator-qubit circuit shown in Figure 2.11. The Hamiltonian in the rotating wave approximation takes the form of a Jaynes-Cumming Hamiltonian with qubit-resonator coupling terms for each qubit

$$\widehat{H} = \hbar\omega_r\hat{a}^\dagger\hat{a} + \hbar\sum_i\frac{\omega_i}{2}\hat{\sigma}_{z,i} + \sum_i\hbar g_i(\hat{a}\hat{\sigma}_{+,i} + \hat{a}^\dagger\hat{\sigma}_{-,i}). \tag{2.29}$$

This Hamiltonian is known as the Tavis-Cumming Hamiltonian and describes the coupling of multiple qubits to a single resonator. As for readout we want to be in the dispersive limit where both qubits are far detuned from the resonator. In the dispersive limit the Hamiltonian can be written as [53]

$$\widehat{H} = \hbar\left(\omega_r' + \chi_1\hat{\sigma}_{z,1} + \chi_2\hat{\sigma}_{z,2}\right)\hat{a}^\dagger\hat{a} + \sum_{i=1}^{2}\frac{\hbar\omega_i'}{2}\hat{\sigma}_{z,i} + \hbar g_1 g_2\frac{\Delta_1+\Delta_2}{2\Delta_1\Delta_2}(\hat{\sigma}_{+,1}\hat{\sigma}_{-,2} + \hat{\sigma}_{-,1}\hat{\sigma}_{+,2}), \tag{2.30}$$

where $g_i = \frac{2eC_{gi}}{\hbar C_i}\langle 1|_i\hat{n}_i|0\rangle_i V_{\mathrm{ZPF}}$ and $\Delta_i = \omega_i - \omega_r$. The coupling term is the same as for the direct coupling with a strength determined by the qubits coupling to the resonator and how far detuned the two qubits are. When the two qubits are on resonance the coupling strength is $g_1 g_2/\Delta$.

It turns out that the qubit-qubit coupling term for both schemes has the same form. In Figure 2.12 the level spectrum for two coupled qubits are shown. In blue we see the

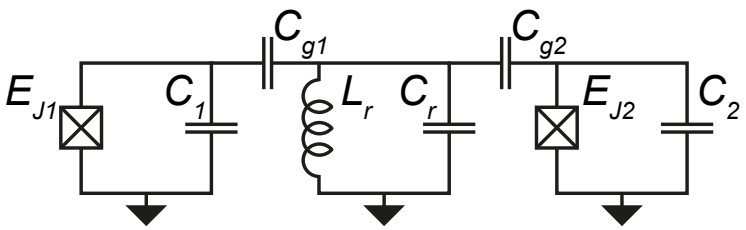

Figure 2.11: Two transmon qubits coupled via a resonator.

expected avoided crossing as the states $|01\rangle$ and $|10\rangle$ hybridize when the two qubits are on resonance. Here $|01\rangle$ refer to the two-qubit state $|0\rangle_1 \otimes |1\rangle_2$. By pulsing diabatically into the anticrossing for a certain time one can perform a iSWAP operation. The iSWAP operation swaps the two qubit states and adds a phase of $-i$ if they are different:

$$\begin{aligned} |00\rangle \to |00\rangle, \quad |11\rangle \to |11\rangle, \\ |01\rangle \to -i|10\rangle, \quad |10\rangle \to -i|01\rangle. \end{aligned} \tag{2.31}$$

The gate set of iSWAP and single qubit gates is in fact a universal gate set [54].

As you might expect by the higher energy modes shown in the figure (red lines) this is not the full story. Recall that the transmon is only a weakly anharmonic oscillator. That is, the transition from the first to the second excited state of qubit 2 will come into resonance with qubit 1 as it approaches the $|01\rangle - |10\rangle$ anticrossing. One can calculate that all states that differ by one excitation couple strongly [16]. That is one excitation can move between the qubits if the energy is conserved. We find an anticrossing when qubit 1 is detuned by the anharmonicity of qubit 2 so that the states $|11\rangle$ and $|02\rangle$ will be on resonance.

With these additional avoided crossings in mind let us revisit the iSWAP gate that we described earlier. Consider what happens if we perform an iSWAP gate on the state $|11\rangle$. At first the two qubits are detuned with Qubit 1 at 4.5 GHz (left in Figure 2.12). Then the frequency of Qubit 1 is changed to 5 GHz so that it is on resonance with Qubit 2. After a certain time the iSWAP gate has been performed and the frequency of Qubit 1 is brought back down to 4.5 GHz. A correct iSWAP should leave the state $|11\rangle$ untouched. However, during the operation the state will go through an avoided crossing with the $|02\rangle$ state. Due to the $|11\rangle$-$|02\rangle$ coupling there will be a finite probability for being in state $|02\rangle$ after the gate. The state $|02\rangle$ is not a qubit state and constitutes an error on our qubits.

At first glance this might not seem like a big problem. We just need to make sure to not perform two-qubit operations using the $|01\rangle$-$|10\rangle$ anticrossing when we are in the state $|11\rangle$. However, in a quantum computer we also want to perform gates on states like $(|01\rangle + |11\rangle)/\sqrt{2}$. Here we cannot reliably perform a iSWAP gate without mixing the states $|11\rangle$ and $|02\rangle$. This is a detrimental problem for the iSWAP gate in transmons that effectively makes it unusable.[12]

[12] In some cases it can be used for state preparation where the $|11\rangle$ state is not present.

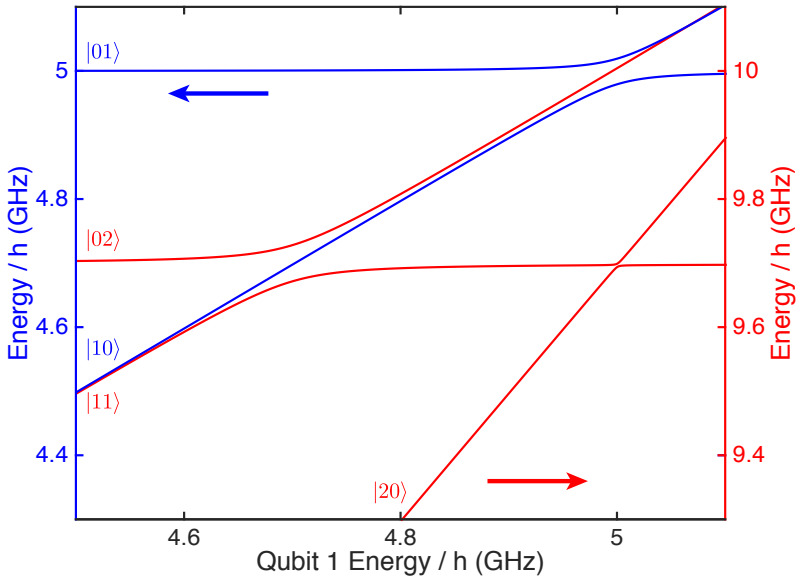

Figure 2.12: Energy levels of a two-qubit system when the energy of the first qubit is being swept. Blue indicates the one-excitation manifold with the energy shown on the left axis. In red the is two-excitation manifold with energy shown on the right axis. In these simulations qubit 2 had energy $E/h = 5$ GHz, the anharmonicity of both qubits was $\alpha = -300$ MHz, and the coupling strength between $|01\rangle$ and $|10\rangle$ was 20 MHz.

As mentioned earlier, transmons instead use a c-phase gate to form a universal gate set. The c-phase gate flips the sign of $|11\rangle$ while leaving all other states untouched:

$$\begin{aligned} |00\rangle &\rightarrow |00\rangle, \quad |11\rangle \rightarrow -|11\rangle, \\ |01\rangle &\rightarrow |01\rangle, \quad |10\rangle \rightarrow |10\rangle. \end{aligned} \tag{2.32}$$

It can be performed by making use of the $|11\rangle$-$|02\rangle$ anticrossing [55]. To perform a c-phase gate one again starts off resonance with qubit 1 at 4.5 GHz. Then pulsing the qubit frequency adiabatically to the anticrossing (at 4.7 GHz in the figure) a phase is being picked up from changing the qubit frequency for states $|10\rangle$ and $|11\rangle$. Due to the anticrossing $|11\rangle$ picks up phase slightly slower than $|01\rangle$ and by tuning the control parameters one can make the state $|11\rangle$ pick up a phase of -1 while $|01\rangle$ is left unchanged. The c-phase gate avoids crossing any unwanted anticrossings on the way to the anticrossing used to perform the gate making high fidelity operation possible. One has to be careful when using the $|11\rangle$-$|02\rangle$ anticrossing as a diabatic approach will allow the qubit to mix with $|02\rangle$. By carefully tuning and optimization of control parameters it is possible to perform fast c-phase gates with high fidelity suitable for quantum computation [56].

Chapter 3

Measurement Setup and Fabrication

3.1 Fabrication

This thesis has data from five different samples with slight variations in fabrication. All samples feature InAs/Al core/shell nanowires from the same growth. The nanowires have a semiconductor core of ∼75 nm diameter grown by molecular beam epitaxy and have a ∼30 nm thick aluminum shell deposited *in situ*.

Data in Sections 4.1-4.3 is from one sample while Section 4.4 features data from an additional sample fabricated in parallel [29]. These devices are fabricated on high resistivity (>5,000 Ω-cm) silicon with an 87 nm thick thermal oxide. An argon milling cleaning step is performed before depositing 75 nm aluminum by e-beam evaporation. Afterwards gold alignment marks are deposited for e-beam lithography. Control lines, cavities, and qubit islands are formed by wet etching the Al film using an e-beam patterned resist mask. The nanowires are deposited on the device chips by a dry deposition technique as explained in [57]. Windows in a resist mask defined by e-beam lithography ensure only nanowires in the desired area stay on the device. Josephson junctions are then formed by wet etching about 180 nm section of the nanowire to create a superconducting weak link. Deposition of nearby gold marks allows for sub 50 nm alignment of side gate and contacts. Contacts and side gate are e-beam patterned in an MMA/PMMA mask and an argon milling step before deposition removes the aluminum oxide for electrical contact. The contact metal layer consists of a 1 nm thick Ti sticking layer followed by 150 nm Al.

Data in Section 4.4 is from a device fabricated in a similar way so only the differences are mentioned [36]. The substrate is high resistivity silicon without any thermal oxide. Crossovers connecting ground planes across control lines are added before deposition of nanowires. These are formed by deposition of an insulating SiO_2 layer followed by Al electrically connecting each side. The qubit islands and cavities are wet etched as the very last step.

Data in Section 5.2 is from a sample fabricated with control lines and cavities again

wet etched in 100 nm Al deposited on high resistivity silicon with no thermal oxide. Nanowires are contacted as before but with no side gate deposited. An insulating ZrO_2 layer e-beam patterned in MMA/CSAR resist mask is formed by atomic layer deposition on top of the nanowire Josephson junctions followed by an Al top gate.

Data in Section 5.3 is from a sample fabricated by reactive ion etching (CL_2/HBr) the control lines, cavities, and qubit/coupler islands in 100 nm thick Al on high resistivity silicon with no thermal oxide. The cleaning step before deposition of the Al film is lighter than for the other samples. Crossovers are added as mentioned above and nanowires deposited for qubits and couplers. After nanowire etches contacts for all nanowires are deposited together with side gates for qubits. Top gates for couplers are placed on top of ZrO_2 as above.

See Appendix A for detailed fabrication notes for each device.

3.2 Measurement Setup

For measurements the samples are placed in an aluminum box to reduce and stabilize magnetic fields at the sample. The aluminum box is installed inside a copper box to reduce infrared radiation that can produce quasiparticles in the aluminum. The insides of both boxes are covered in black absorptive paint (Aeroglaze Z306) to further reduce infrared radiation. The boxes are placed in a cryo-free dilution refrigerator with a base temperature <50 mK. Installed around the box is a cryoperm magnetic shield.

Control wiring used for data presented in Sections 4.5 and 5.2 is shown in Figure 3.1. Readout input and output lines probe the resonator as shown in Figure 3.2. When measuring resonances of resonators the radio frequency (RF) switch (4 in figure) is flipped so that readout input and output signals go to the vector network analyser (VNA). With a VNA we can map out the transmission across a wide frequency spectrum, convenient when the frequency of the readout resonator moves more than a linewidth.

When doing time domain measurements of the qubit we only need to measure the change in transmission at the resonance frequency (we just want to know if it shifted). For this an RF signal at the resonance frequency is sent to the resonator and the transmission is detected by heterodyne detection. By mixing the transmitted signal with a slightly detuned local oscillator RF source we get a signal at the difference frequency (usually chosen to be around $10 - 30$ MHz). A waveform digitizer samples the intermediary frequency signal followed by digital down conversion.

When measuring two qubits simultaneously, the resonance frequencies of the two readout resonators are slightly different. Two RF signals are combined at room temperature one at each readout resonator's resonance frequency as shown in Figure 3.1. The two device resonators are of the type in Figure 3.2**B** placed in series with a common feedline coupled to both. Each RF signal will probe the resonator it is resonant with and ignore the other one. At room temperature the transmitted signal is mixed with a local oscillator such that the down converted signals are >10 MHz apart. The signals are then separated digitally.

All time domain measurements are controlled by a Tektronix AWG 5014C. This

arbitrary waveform generator (AWG) handles the envelopes of RF signals sent to the sample. By routing the signal from the AWG to the IQ inputs of vector signal generators we can control the amplitude of the in phase and out of phase components of the generated RF signal. These signals control single qubit gates (green) and readout (red) as well as triggering the digitizer for measurement. A single line from the AWG to the nanowire gate allows nanosecond control of the gate voltage (blue). The fast signal is combined with a DC voltage source via an RC bias-T.

There are slight differences to the setup for data presented in Sections 4.1-4.4 and 5.3. For Sections 4.1-4.4 several components are placed at room temperature instead. The single qubit drive signal (green) is combined at room temperature with the readout input signal. The bias-T for the gate control is also placed at room temperature. Furthermore, for sample 1 in Sections 4.1-4.4 the readout signal is mixed down to DC before going to the digitizer. This is done by splitting the readout signal at room temperature. One part is sent to the sample and the transmitted signal mixed with the other part at room temperature. Lastly, there is no cryoperm magnetic shield around the sample.

For the sample in Section 5.3 a traveling waveform parametric amplifier is installed but it is not turned on during measurements. Also single-qubit control is sent to the qubit through the gate line. That is, the qubit control line (green) is combined with the fast gate line from the AWG at room temperature. A thorough description of this setup is given in [44].

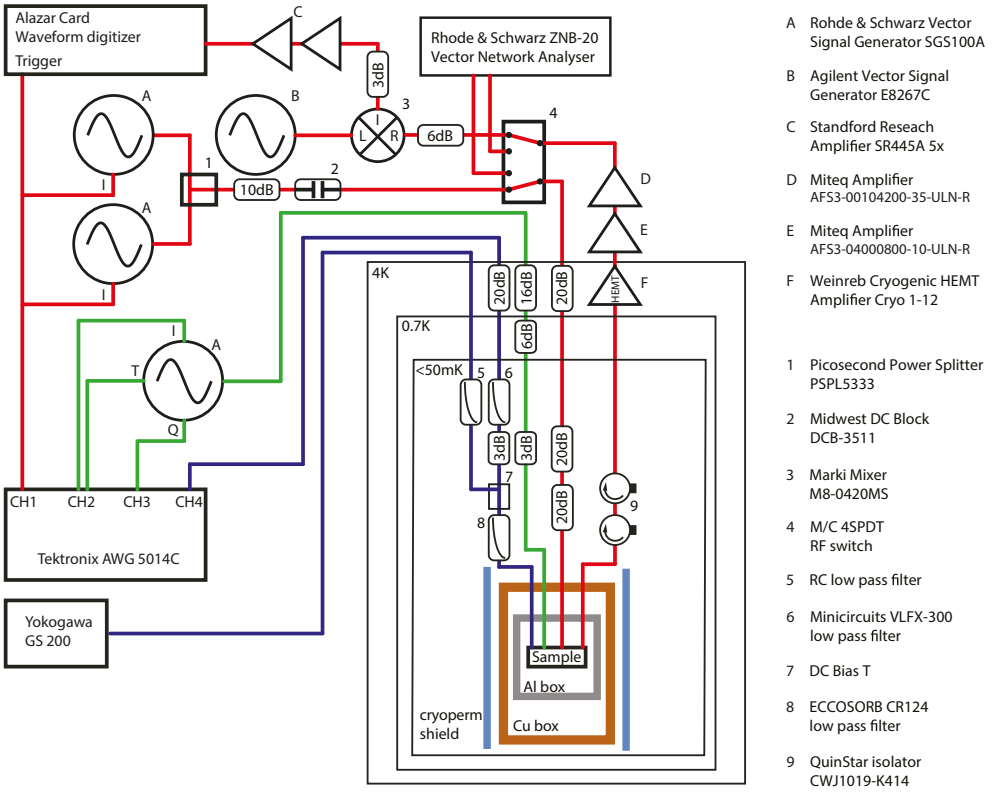

Figure 3.1: Detailed schematics of measurement setup for samples presented in Section 4.5 and Section 5.2. Other samples were measured in slightly different setups as discussed in the main text.

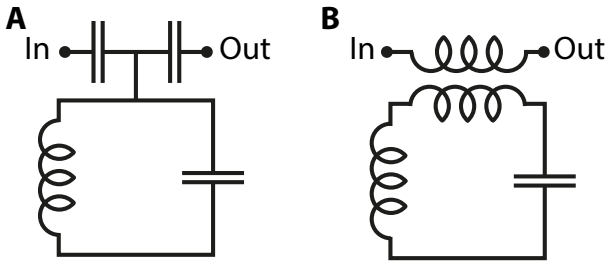

Figure 3.2: Coupling to a resonator for readout. **A** Transmission only allowed at the resonance frequency of the resonator seen as peak in the transmission. **B** Transmission is suppressed at the resonance frequency of the resonator.

Chapter 4

The Gatemon

This Chapter presents data previously published in [29] and [36]. First the physical implementation of a gatemon-resonator system is considered and the coupling strength is probed directly. Then the spectrum of the gatemon is mapped as a function of gate voltage. Coherent control of a gatemon is demonstrated followed by measurements of quantum coherence times. Lastly, a two-qubit coupling between gatemons is implemented.

4.1 Physical Realization

The physical implementation of the resonator-qubit system is illustrated in Figure 4.1. The system is fabricated as two-dimensional structures using an aluminum film on a silicon substrate. The readout resonator is formed by a coplanar waveguide with a center conductor that is broken twice. Such a break forms a capacitor that acts as a weakly transmitting mirror for microwaves. Placing two mirrors a distance apart will form a cavity with standing waves as resonances. Each standing wave is known as a mode of the cavity and can be modeled as a harmonic oscillator. The voltage fluctuations of the lowest mode is indicated in yellow with voltage antinodes at the capacitors. The microwave cavity in Figure 4.1 is a $\lambda/2$ resonator, where λ is the wavelength of the resonance, as the length of the cavity is half the wavelength of the lowest mode. One can also create $\lambda/4$ cavities that are formed by having one end grounded and a capacitor at other end. A capacitor enforces a voltage antinode while a ground enforces a voltage node making the lowest mode a quarterwave. As long as we work with energies well below the second mode, we can model a cavity as a single harmonic oscillator given by the lowest mode. As the resonator is now a distributed element the voltage fluctuations V_{ZPF} becomes spacially dependent [58]. The cavity used in our experiment was a $\lambda/2$ cavity with frequency $f_C = 5.96$ GHz and quality factor $Q = 1500$.

The qubit capacitor is formed by a 'T'-shaped island. From electrostatic simulations we estimate the charging energy of the island to be $E_C/h = e^2/2Ch \approx 200$ MHz. It is placed near the voltage antinode of a microwave cavity as the cavity-qubit coupling scales with the voltage fluctuations in the resonator. To complete the gatemon circuit the

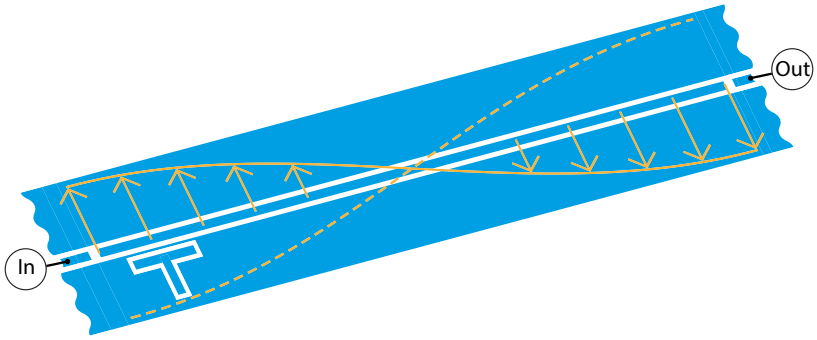

Figure 4.1: A microwave cavity formed by two breaks in the center conductor of a coplanar waveguide. The cavity can be modeled as a single mode resonator allowing us to treat it as a simple LC harmonic oscillator. The 'T'-shaped island constitutes the capacitor of a transmon circuit.

qubit island is shorted to the ground plane through a semiconductor-nanowire Josephson junction. Figure 4.2**A** shows an SEM image of the nanowire Josephson junction used for the first gatemon sample. In Figures 4.2**B** and **C** optical images show the contacts to the nanowire and nearby gate electrode. The gate electrode allows tuning of the Josephson energy through the semiconductor. We estimate the critical current of the nanowire to be $I_c = eE_{01}^2/4E_C\hbar = 25$ nA for $E_{01}/h = 4.5$ GHz. From spectroscopy data we estimate the anharmonicity to be $\alpha/h \approx -100$ MHz which is consistent with a few highly transmitting modes in the nanowire Josephson junction.

A schematic of the resonator-qubit system is shown in Figure 4.2**D**. The frequencies of the microwave signals used to control and readout the qubit are indicated as f_C and f_Q. For readout, f_C probes the cavity frequency while f_Q induces qubit rotations. The qubit control signals are applied to the resonator and not directly to the qubit which was considered in Section 2.4. Effectively this lowers the drive strength seen by the qubit as the resonator acts as a bandpass filter [38]. This is compensated for simply by increasing the power of the drive.

4.2 Vacuum Rabi Splitting

To directly measure the qubit-cavity coupling the gatemon is tuned with the gate voltage into resonance with the lowest mode of the cavity. This is the resonant regime of the Jaynes-Cumming Hamiltonian. In Figure 4.3**A** the cavity response is shown as a function of gate voltage and cavity drive frequency for low driving power. We observe two transmission peaks in the cavity aperiodically modulated by the gate voltage on the gatemon. The aperiodicity is consistent with mesoscopic fluctuations in the conductance of the nanowire junction. The two peaks are the hybridized cavity-gatemon states [59]. The observation of two clear peaks, Figure 4.3**B**, indicates that we are in the strong coupling regime with g larger than both the lifetime of the qubit and the cavity. The strong hybridization of both states with the cavity allows us to probe them by probing the cavity. Off resonance the qubit-cavity states are very weakly hybridized and we only

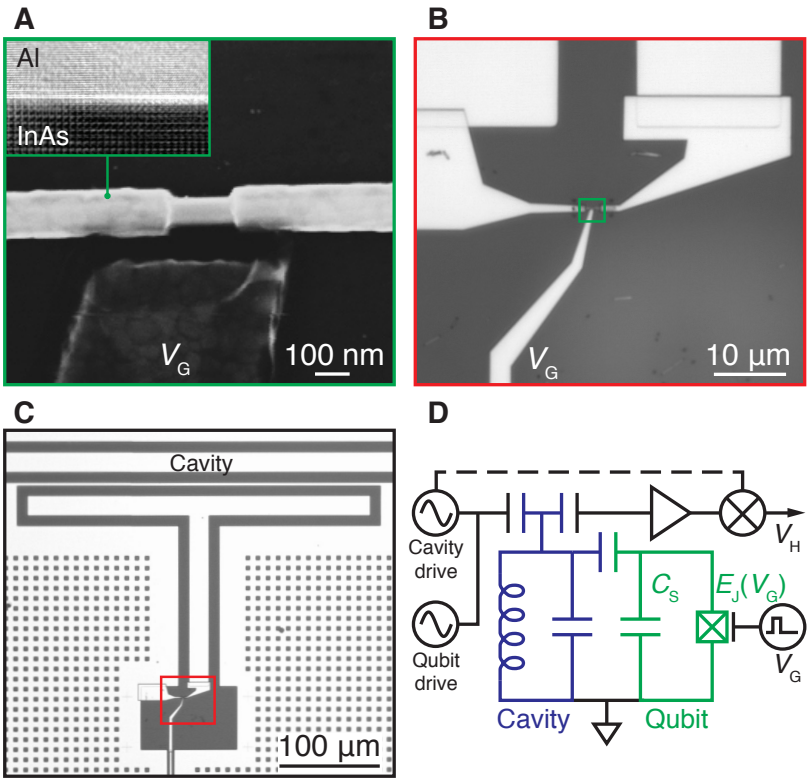

Figure 4.2: **A** The nanowire Josephson junction integrated into a transmon circuit. **B** The nanowire is contacted at each end and a nearby gate electrode can tune the Josephson energy of the junction. **C** The transmon is formed by a T-shaped island shorted to the surrounding ground plane through the nanowire Josephson junction. The transmon circuit is closed by the capacitance of the island to ground. The island is capacitively coupled to a $\lambda/2$ microwave cavity for readout. **D** Schematic of the gatemon circuit.

observe one peak, the cavity resonance. We cannot measure the pure qubit eigenstate directly.

To better estimate the coupling strength g we extract the peak splitting δ for each voltage value with two peaks in 4.3**A**. The hybridized states, $f_{\pm}$, can be calculated from the coupling strength g,

$$f_{\pm} = \frac{f_Q + f_C \pm \sqrt{(f_Q - f_C)^2 + 4(g/2\pi)^2}}{2}, \tag{4.1}$$

where f_C and f_Q are the frequencies of the uncoupled cavity and qubit respectively. By plotting the peak splitting $\delta = f_+ - f_- = \sqrt{(f_Q - f_C)^2 + 4(g/2\pi)^2}$ as a function of f_Q as shown in Figure 4.3**C** we extract a coupling strength $g/2\pi = 99$ MHz. Plotting the data in 4.3**A** parametrically as a function of the extracted f_Q the expected avoided crossing of a coupled two-level system is revealed in Figure 4.3**D**.

4.3 Coherent Manipulation

To perform coherent operation on the gatemon, we detune it away from the cavity frequency to the dispersive regime. While continuously monitoring the cavity transmission at the cavity frequency we sweep a second microwave tone to drive the qubit. When the qubit drive, the second tone, hits the resonance frequency of the qubit, the qubit is excited into an incoherent superposition of $|0\rangle$ and $|1\rangle$ which modulates the monitored cavity transmission. By sweeping the frequency of the qubit drive and the gate voltage we map out the spectrum of the gatemon in Figure 4.4. In the spectrum we directly observe the aperiodic modulation of the gatemon frequency originating from mesoscopic fluctuations in the nanowire. These fluctuations create local minima and maxima that are first-order insensitive to gate voltage (sweet spots). We also observe discontinuous jumps in the spectrum that we attribute to charge traps near the nanowire changing the charge landscape. Such jumps rarely happen when the gate voltage is restricted to a small voltage range.

The data shown in Figure 4.4 does not reveal the exact qubit spectrum as there is a Stark shift on the qubit due to photons in the cavity. The Stark shift changes the qubit frequency but the observed response to the gate is not changed. By modulating the readout and drive in time instead of continuous drive and measurement one can completely eliminate the Stark shift. This is done for all later data in this thesis.

Figure 4.5**A** shows a scan of the qubit spectrum around the sweet spot at 3.4 V. Spectroscopy is performed by first applying a 2 μs long qubit drive tone and then probing the cavity response to avoid Stark shift in the data. To perform qubit operations on the gatemon we fix the gate voltage at 3.4 V indicated by B. In the top panel of Figure 4.5**B** the pulse scheme for Rabi oscillations is shown. First a qubit drive tone of length τ rotates the qubit about the X axis and then a readout tone measures the probability for the qubit to be in the $|1\rangle$ state. The lower part of the main panel shows Rabi oscillations as the qubit is rotated around the Bloch sphere. When the qubit drive is detuned from the resonance frequency the qubit does not fully reach the $|1\rangle$ state. The rotation axis

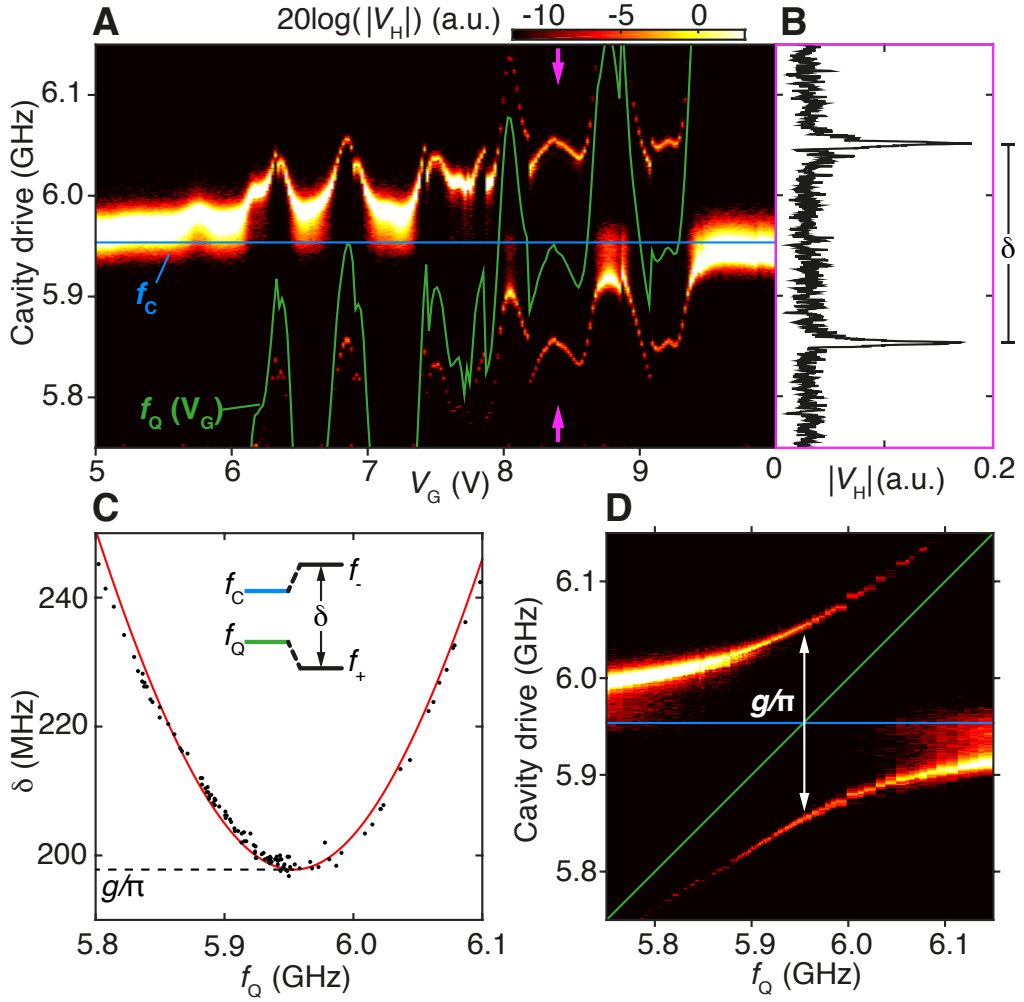

Figure 4.3: **A** Hybridization of the microwave cavity and gatemon qubit. Extracted qubit frequency and cavity frequency shown as green and blue lines respectively. **B** Line cut of A indicated by purple arrows. Clearly separated peaks in the transmission. **C** The vacuum Rabi splitting as a function of extracted qubit frequency. **D** Parametric plot of the vacuum Rabi splitting as a function of extracted qubit frequency reveals the expected anticrossing of two hybridized states.

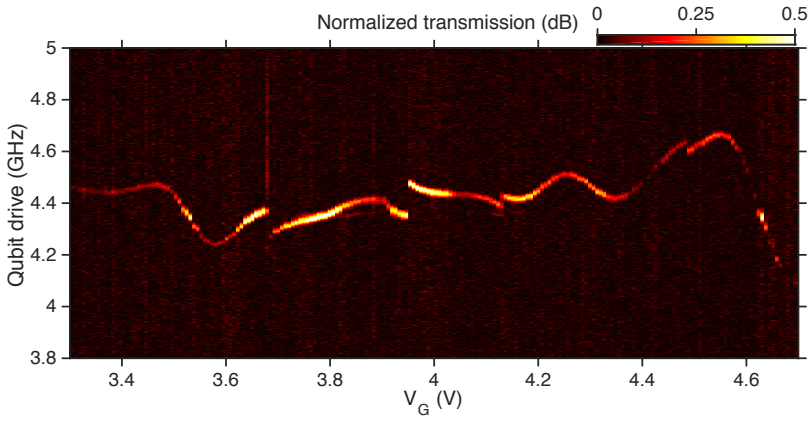

Figure 4.4: Spectroscopy measurements of the qubit frequency as a function of gate voltage. Each column is normalized by the value at 3.8 GHz.

is pushed off the X axis due to a $\hat{\sigma}_z$ contribution in the drive which also increases the rotation frequency (see equation (2.21)). By sweeping the drive time and drive frequency we can see the effect as the Chevron pattern in the main panel.

While drive pulses around axis in the XY pane are enough to perform all single qubit operations it is convenient to have fast control of the qubit frequency to perform two-qubit operations. To show that the gatemon allows fast adiabatic pulses of the qubit frequency we measure the effect on a single qubit. Changing the qubit frequency effectively induces Z rotations on the Bloch sphere as seen in Equation (2.18). The operations are simplified by placing the gate voltage at 3.27 V where the qubit frequency depends linearly on the gate voltage. This ensures that the rotations induced by the change in frequency depend linearly on the gate voltage. To observe rotations, we first rotate the qubit by $\pi/2$ to the equator of the Bloch sphere as shown in the upper panel of Figure 4.5**C**. Then a gate pulse of length τ induces a rotation around the Z axis with a frequency proportional to the pulse amplitude (due to the linear energy spectrum). A final $\pi/2$-pulse allows effective readout along the Y axis of the Bloch sphere. In the main panel we see the rotations that depend on the length of the pulse and the amplitude of the voltage pulse on the gate. Furthermore, these operations demonstrate the stability of the gatemon as the data in the main panel of Figure 4.5**B** were collected over several hours.

4.4 Coherence Times

In Figure 4.6 coherence measurements of two gatemon qubits are shown. The pulse schemes for measuring the lifetime T_1 and dephasing time T_2^* are shown in black and blue respectively. Lifetime is measured by varying the delay time between a π pulse that rotates the qubit to the $|1\rangle$ state and readout. The expected exponential decay with a characteristic time T_1 of the $|1\rangle$ state probability is observed. We extract lifetimes 0.56 μs and 0.83 μs for sample 1 and 2 respectively.

The dephasing time is measured by placing the qubit on the equator with a slightly

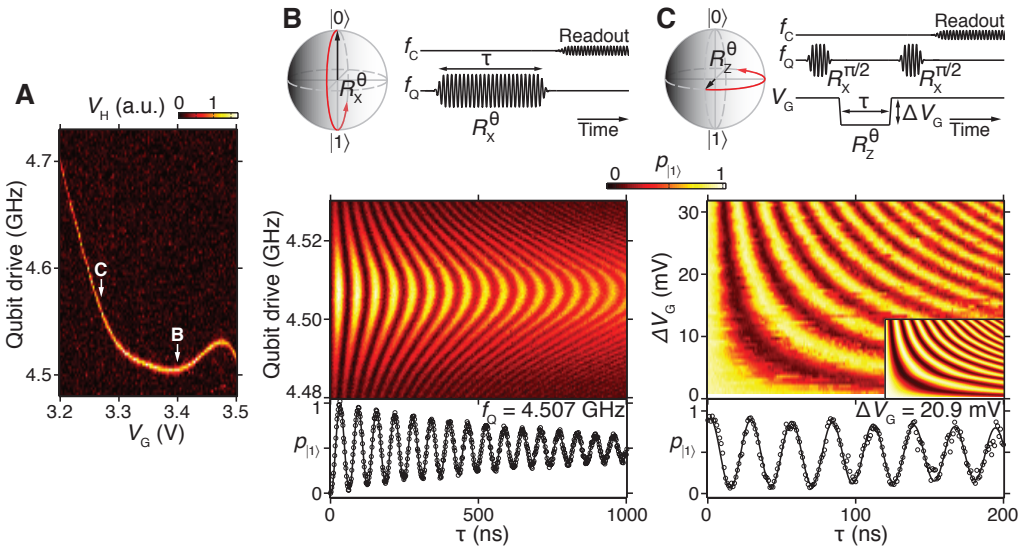

Figure 4.5: **A** Spectroscopy of the gatemon. **B** Upper panel shows the pulse sequence for qubit rotations around the X axis on the Bloch sphere. Main panel shows Rabi oscillations as a function of drive time τ and qubit drive frequency. Lower panel is a line cut at the qubit frequency. **C** The pulse sequence for Z rotations is shown in the upper panel. Main panel shows rotations as a function of drive time τ and gate pulse amplitude. Lower panel is a line cut for at the qubit frequency. Normalized state probability, $p_{|1\rangle}$, is calculated from the demodulated cavity response, V_H, by fitting Rabi oscillation to an exponentially damped sinusoid of the form $V_H^0 + \Delta V_H \exp(-\tau/T_{\text{Rabi}}) \sin(\omega\tau + \phi)$ to give $p_{|1\rangle} = (V_H - V_H^0)/2\Delta V_H + 1/2$. The solid curves in lower panels of A and B are exponentially damped sinusoids.

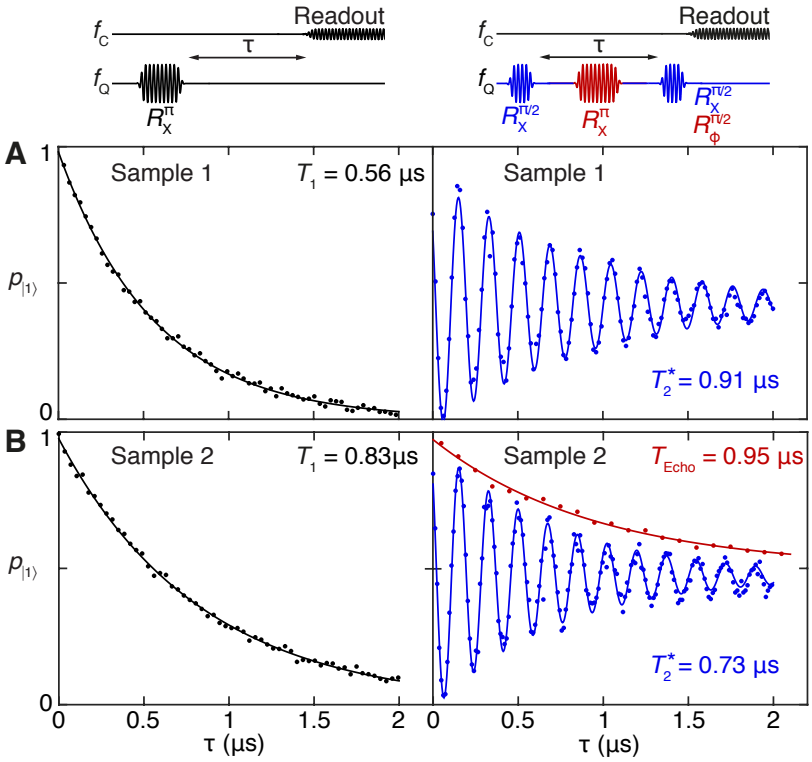

Figure 4.6: **A** Left shows lifetime measurement of sample 1 at point B in Figure 4.5**A** ($V_G = 3.4$ V). Left side in upper panel shows the pulse scheme for lifetime measurements. A 30 ns π pulse rotates the qubit to the $|1\rangle$ state and a wait time τ before readout is varied. Solid curve is an exponential fit. Right side shows a Ramsey experiment performed by varying a wait time τ between two slightly detuned 15 ns $\pi/2$ pulses. Solid curve is an exponentially damped sinusoid from which we determine T_2^*. **B** Lifetime and Ramsey experiments are repeated for sample 2 which has $f_Q = 4.426$ GHz ($V_G = -11.3$ V). Furthermore we perform a Hahn echo experiment in red with a π pulse inserted between two $\pi/2$ pulses with a varying wait time τ. The phase of the second $\pi/2$ pulse is varied to fit an exponential decay to the extracted amplitude.

detuned $\pi/2$ pulse so that the qubit state precesses around the equator. Readout is done after a delay time τ and second $\pi/2$ pulse to rotate the Y axis onto the Z axis for readout. We observe the precession of the qubit as the oscillation while the exponential decay with a characteristic time scale T_2^* is due to dephasing. Lifetime enforces an upper limit on the dephasing time of $T_2^* \leq 2T_1$ as the qubit can decay from the superposition state on the equator. For Sample 1 we find $T_2^* = 0.97$ μs very close to the lifetime limit. Sample 2 performs slightly worse with $T_2^* = 0.71$ μs. For drifts in the qubit frequency that are constant within the time of the pulse sequence one can cancel the effect by performing an echo pulse as indicated in red. The pulse effectively reverses the sign on the noise such that noise picked up before the echo pulses is canceled by noise after the pulse. High frequency noise switching faster than the sequence length will not get canceled by an echo pulse. More elaborate pulse schemes can be used to avoid dephasing noise in the system [60]. We can increase the dephasing time of qubit 2 to $T_{\text{Echo}} = 0.95$ μs with an echo pulse. The fact that we do not reach the lifetime limit indicates that qubit 2 suffers from some high frequency noise.

The measured lifetimes are much lower than state of the art transmons of T_1 ∼30-40 μs [25]. A big limitation for lifetimes in these first generation gatemon samples is the lossy 87 nm SiO_2 layer on the wafer. The next generation of gatemon samples is made on silicon wafers with only the native oxide layer. Furthermore, the general fabrication is cleaner and a magnetic shield is added to the measurement setup. These factors together allows improvement of the coherence times to $T_1 = 5.3$ μs and $T_{\text{Echo}} = 9.5$ μs [36]. Future work will involve meticulously going through our fabrication process and setup to find limiting factors in the system.

4.5 Two Qubit Gates with Gatemons

The first demonstrations of qubit-qubit couplings for transmon qubits were performed with couplings mediated via microwave cavities [52, 61]. Such coupling schemes are still widely used in state of the art experiments [19, 62]. As well as improved coherence times, our second gatemon sample features a capacitive two-qubit coupling. The measured sample is shown in Figure 4.7. Several improvements were made in the design layout. We separate drive lines from the readout to have individual gatemon control. The drive lines are labeled 'XY control', and are coupled capacitively to each qubit. For readout each qubit is coupled to a $\lambda/4$ microwave cavity. Both cavities are coupled to the same microwave feedline (not shown) but have slightly different resonance frequencies to allow frequency-multiplexed, simultaneous readout. The qubit parameters differ only slightly from the first generation of gatemons with simulated values of charging energy $E_C/h =$ 230 MHz and qubit-cavity coupling $g/2\pi \approx 100$ MHz. The cavities have resonance frequencies ~ 8 GHz to avoid Purcell limits.

The two qubit coupling is engineered simply by placing the two qubits close to each other. Electrostatic simulations predict a coupling strength $J \sim 20$ MHz. To directly observe the coupling, the qubits are brought into resonance. In Figure 4.8**A** we observe an avoided crossing as Q1 is swept through the resonance frequency of Q2.

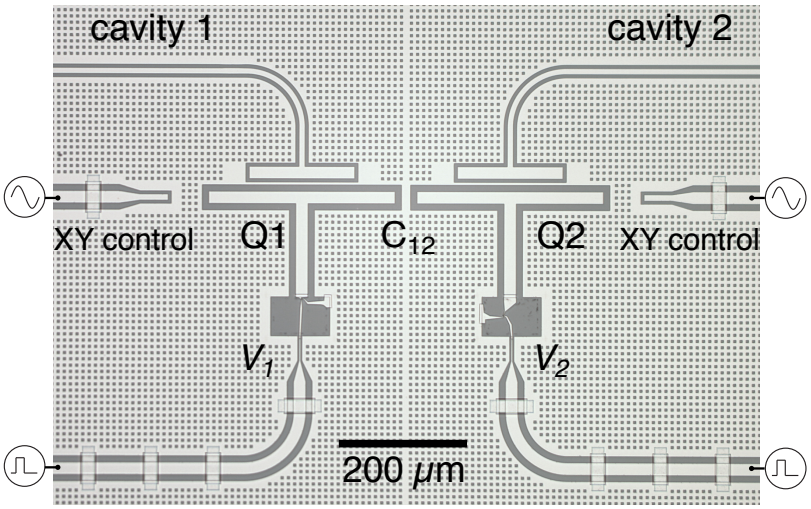

Figure 4.7: Optical image of a two qubit gatemon device. The two qubits are coupled to individual $\lambda/4$ cavities. Coherent operations are performed by drive lines coupled capacitively to the gatemons.

To demonstrate that we have full coherent control of the two-qubit system we perform coherent iSWAP operations. The applied pulse sequence is shown in 4.8**B**. With the qubits initially detuned a single π pulse on Q2 excites the qubit to the $|1\rangle$ state while Q1 is left in the ground state. A gate voltage pulse with amplitude ΔV_2 on Q2 brings the qubits diabatically into resonance and waiting for a time τ before bringing the system back for readout. The excitation that started out on Q2 begins to oscillate between the hybridized qubits with a frequency J/π. The $|1\rangle$ state probability in Q1 after an iSWAP operation is mapped out as a function of waiting time τ and pulse amplitude ΔV_2 in Figure 4.8**C**. A chevron pattern is observed as the excitation coherently swaps between Q1 and Q2. A similar plot is obtained for measurements of the $|1\rangle$ state probability of Q2 which is inverted compared to 4.8**C**. In 4.8**D** a line trace of both measurements is shown demonstrating the excitation swapping between the two qubits. From the oscillations we extract a coupling strength of 17.8 MHz. The deviation from the simulated value might be explained by a slight over etch of the islands in the fabrication. Smaller islands decrease the capacitance between the islands and thereby lower the coupling.

While the data in Figure 4.8**C** looks very similar to the single qubit drive data in Figure 4.5 the qubit states are very different. If the state of both qubits had been measured in a single shot then we would find a perfect anti-correlation between the two qubit states. The system starts out with one excitation and there is exactly one excitation in the combined system after the iSWAP operation independent of the probability for the excitation to be on one qubit. These qubit-qubit correlations are the hallmark of entangled quantum states. We did not have single-shot measurements on this device but recently single-shot measurement were implemented on gatemons taking the first steps towards two-qubit correlation measurements [44].

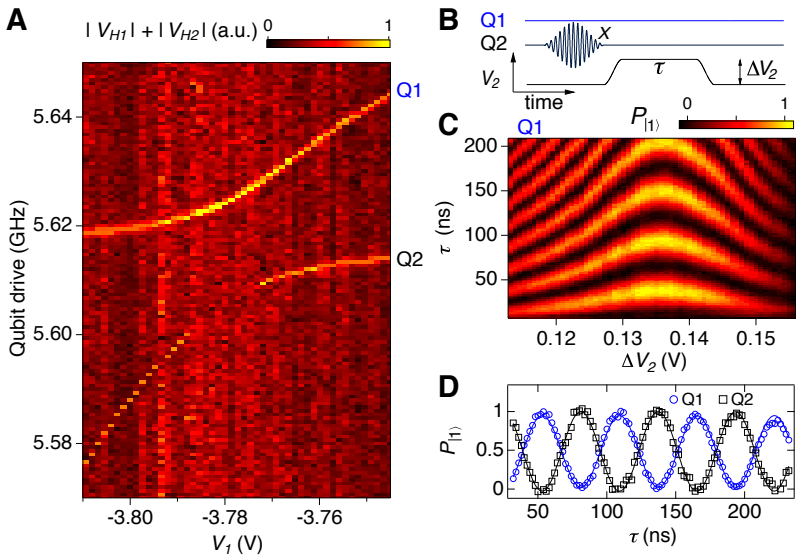

Figure 4.8: **A** An avoided crossing is observed in spectroscopy measurements as the frequency of Q1 is being swept through the frequency of Q2. **B** Pulse sequence for mapping the qubit-qubit coupling in time domain. Q2 is excited by a π pulse followed by a gate pulse with amplitude ΔV_2 and width τ. **C** Swap oscillations as a function of ΔV_2 and width τ. **D** Line cut of **C** with the gate pulse bringing the qubits into resonance for time τ.

Chapter 5

Towards Tunable Qubit-Qubit Coupling

This chapter considers the possibilities for other applications of nanowire Josephson junctions, specifically implementing a tunable coupling architecture. First, a nanowire based superconducting switch is proposed. The switch is then implemented in two different coupling schemes that allow control of the qubit-qubit coupling strength. The first is based on a tunable cavity while the second is based on an effective tunable coupling capacitance.

5.1 A Nanowire Switch

So far we have implemented the nanowire Josephson junction as a tunable, non-linear inductor to form qubits. However, with such unique and new circuit elements at hand, it is worth considering other applications for gate tunable junctions. A unique feature of a gate tunable Josephson junction is the ability to pinch off the semiconductor junction ensuring that no supercurrent can flow. Standard tunnel junction can also be tuned in SQUID geometries but a Josephson junction that can be completely turned off cannot be reliably fabricated due to small variations in fabrication.

By placing several nanowire Josephson junctions in parallel it is possible to create large on state critical current while being able to turn it off completely with a single gate voltage. A top gate is used to bring the gate closer to the nanowire. The nanowire should go from conducting to pinched off in the smallest voltage range possible. Such a set of 6 junctions are illustrated in Figure 5.1 with overlaid contacts in blue and top gate in red. By contacting every second aluminum patch from each side we effectively have all 6 junctions in parallel forming a single Josephson junction.

As the Josephson inductance scales inversely with the Josephson energy the effective junction inductance will be very low. If large enough Josephson energies are reached the effective impedance of the junction, $Z \propto \omega L \propto \omega / E_J$, will be much smaller than the characteristic impedance of the system (50 Ω). When the semiconductor junction

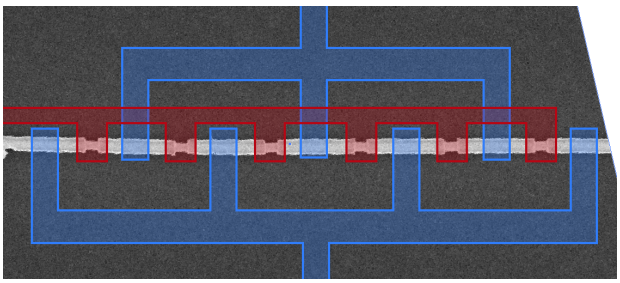

Figure 5.1: SEM image of multiple Josephson junctions etched on the same nanowire. Contacts are illustrated in blue. A top gate (red) placed on top of the junctions tune the conductance in the semiconductor.

allows a large critical current to flow, the switch is closed, while it is open when the semiconductor is pinched off. These two regimes together form a voltage controlled, superconducting switch.

A natural place to implement such a superconducting switch is a controllable qubit-qubit coupling where a digital on-off is desirable. The pinched off state of a nanowire switch is very stable - the critical current is *zero*. However, it will have a varying critical current in the 'on' state, that is the critical current is susceptible to charge noise in the gate. A coupling term between qubits has to be very stable over long times to allow high fidelity two-qubit gates. Therefore, we would like the pinched off state of the switch to enable a qubit-qubit interaction. It is less of a problem to have the qubit-qubit coupling fluctuate slightly in the off state as it (hopefully) is very small - if not zero.

5.2 Switchable Cavities

A good place to start when considering a tunable qubit-qubit coupling is the theory describing the coupling. The coupling strength of two qubits on resonance coupled via a cavity is described by the Hamiltonian,

$$\widehat{H}_{QQ} = \frac{g_1 g_2}{\Delta}(\hat{\sigma}_{+,1}\hat{\sigma}_{-,2} + \hat{\sigma}_{-,1}\hat{\sigma}_{+,2}), \tag{5.1}$$

where $g_i = \frac{2eC_{gi}}{\hbar C_i}\langle 1|_i \hat{n} |0\rangle_i V_{\mathrm{ZPF}}(x)$ and $\Delta = \omega_i - \omega_r$. The coupling strength g_i depends on the position of the qubit, x, along the cavity as the zero point fluctuations $V_{\mathrm{ZPF}}(x)$ in the cavity depends on the position of voltage nodes and antinodes. One way to control the coupling is to change the boundary conditions of a cavity. This will change the position of voltage nodes and antinodes as well as the resonance frequency. If done correctly, one can make the two effects work together to maximize the on-off ratio of the tunable qubit-qubit coupling.

Consider the two cavities in Figure 5.2. While both resonators have the same length, the resonance frequencies differ by a factor of two due the different boundary conditions. Also the voltage fluctuations along the resonator differ dramatically as one end is either a voltage node or antinode. If we place two qubits as indicated, they will couple strongly in the case of 5.2**A** while they couple weakly for 5.2**B** due to the change in V_{ZPF} at

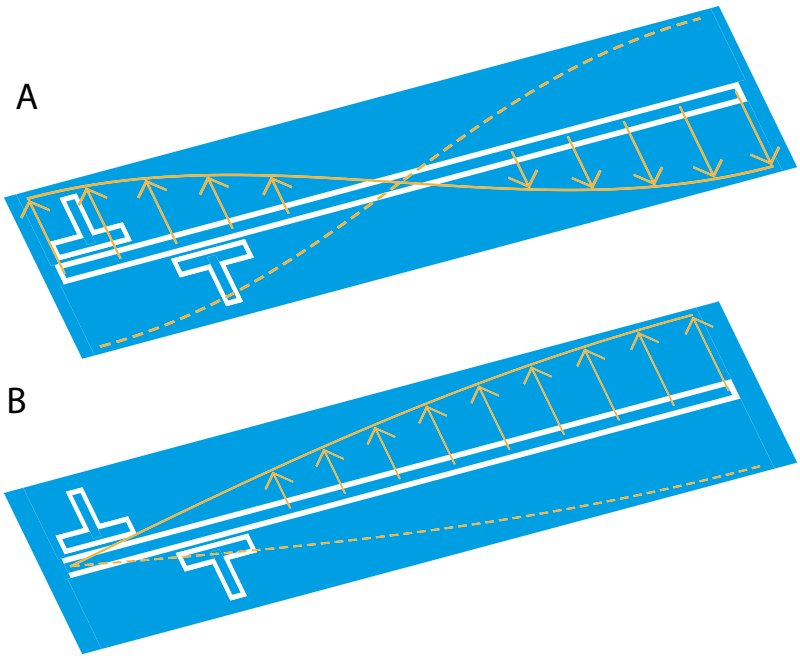

Figure 5.2: **A** An illustration of the zero point fluctuations in the electrical field for a $\lambda/2$ cavity. Two qubit islands couple strongly to the cavity at the voltage antinode. **B** Same as **A** but for a $\lambda/4$ cavity. The two qubit islands couple weakly to the cavity at the voltage node.

the qubit position. Now consider the two cases as the limits of a single cavity with a superconducting switch at one end. In the pinched off state (open switch) the nanowire forms a capacitor and will have a voltage antinode as in 5.2**A**. This is the 'on' state of the coupling as we wanted. Closing the switch will force a ground at the nanowire position turning off the coupling as shown in 5.2**B**. Placing the qubit frequencies above that of the resonator frequency will allow an increase in Δ when the switch is closed.

The arguments above also hold for a cavity grounded in the end opposite the nanowire. However it will be a $\lambda/4$ cavity in the 'on' state and $\lambda/2$ cavity in the 'off' state - opposite the one above. Placing the qubits below the resonance frequency of the cavity in the on state will allow an increase in Δ as the resonator goes from the 'on' to the 'off' state.

To test the switchable cavities we fabricate a sample with cavities of both types, see Figure 5.3**A**. The lengths are adjusted such that the resonance frequencies of the cavities are near 6 GHz when the nanowires are pinched off. The measured resonances as a function of the switch voltage on the nanowire are shown in Figures 5.3**B** and **C**. We clearly observe a resonance at far negative voltages on the switch as expected. Below a certain threshold, when the nanowire is pinched off, going further negative does not affect the system. This is the expected voltage insensitive regime where the nanowire is pinched off. Above the threshold voltage the resonance starts moving as the nanowire becomes conducting and a Josephson junction forms. The cavities' resonance both moves and becomes weaker with higher switch voltage. The weaker response is consistent with

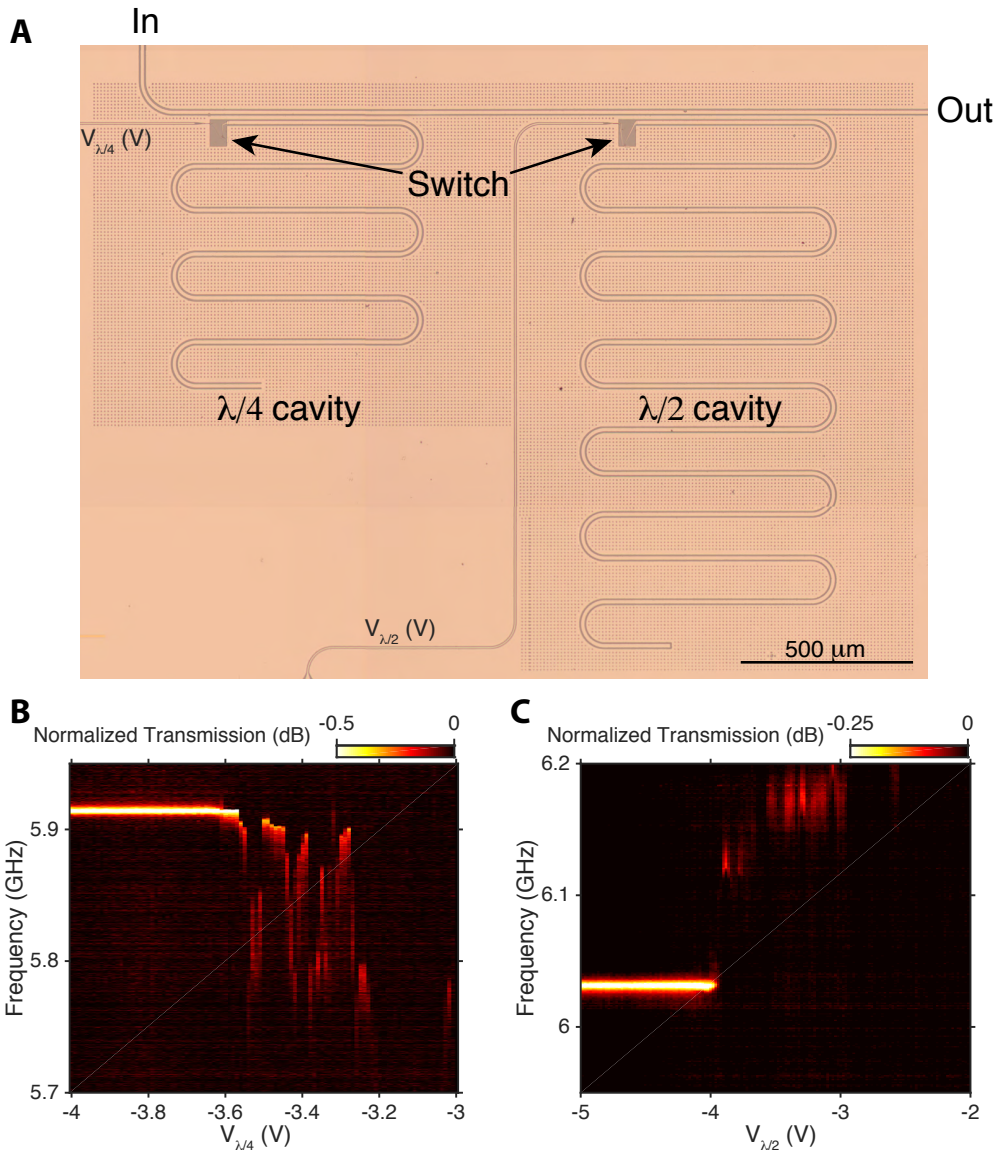

Figure 5.3: **A** Optical image of a device with tunable resonators. Left (right) is a $\lambda/4$ ($\lambda/2$) cavity with a nanowire switch connecting to the surrounding ground plane in the top. Both cavities are coupled to the same microwave feedline but has slightly different resonance frequencies. Data is normalized to the right most column. **B** The resonance of the $\lambda/4$ cavity as a function of switch voltage. **C** Same as **B** but for a $\lambda/2$ cavity.

the voltage antinode being moved, which will induce a modulation on the coupling to the feedline. However, the frequency change is the opposite of what we expect - we expect the $\lambda/2$ cavity to go down in frequency as illustrated in Figure 5.2. Although we currently do not have an explanation for this response, the data strongly suggest that the qubit-qubit coupling can be modulated by a nanowire switch. These results encourage further experiments with qubits to measure the qubit-qubit coupling directly as a function nanowire switch gate.

We also measure quality factors of the resonators to estimate the Purcell limit of a qubit that might be coupled to it. The quality factor of a control resonator with no nanowire switch is measured to 50 000, which is slightly lower than a standard resonator fabricated in the group at the time. The degraded quality factor on this sample can be explained by a very rough aluminum etch of cavities and control lines. However, quality factors of the tunable resonators are measured to be $\sim$2 000 which will compromise qubit performance. The low quality factor may be explained by extra unwanted oxide layers on the chip necessary due to the rough etch to ensure that the gate electrodes are isolated from the ground plane. Recent results in the group have shown quality factors up to 300 000 for tunable resonators which is well above Purcell limiting the qubit for reasonable detunings.

5.3 Switchable Couplers

Going back to Equation (5.1), we consider a different approach to tunable coupling aimed at the capacitance C_{gi}. A capacitance is defined by geometric factors which are hard to change *in situ*. To effectively control the capacitance we add an extra island, a coupler, shown schematically in Figure 5.4. By introducing a switch to the coupler, we can lower the capacitance between the resonator and qubit by grounding the island. When the switch is open the qubit couples to the cavity with a reduced strength. The strength is reduced both due to the coupling going through two capacitors in series and due to the coupler's capacitance to ground which acts as a voltage divider. The decrease in coupling strength can be compensated by increasing the capacitance of the qubit and cavity to the coupler while decreasing the couplers capacitance to ground as much as possible. When the switch is closed the coupler is grounded and only the residual direct capacitance between qubit and cavity is left. This type of coupling could also be employed directly between qubits.

To test the idea, we fabricate samples with three qubits each with an individual coupler to a common cavity, see Figure 5.5. The qubits are 'Y'-shaped islands to increase the capacitance to the couplers. The cavity has 'fins' around the couplers also for increased capacitance. The length of the coupler is maximized to reduce the residual capacitance between the qubit and resonator. The length is limited by its capacitance to the surrounding ground plane which increases as it becomes longer, lowering the maximal coupling strength between qubit and cavity. To combat the increasing capacitance to ground the coupler is kept very thin between the qubit and the cavity and the ground plane is removed near the coupler. Electrostatic simulations showed an on/off ratio of

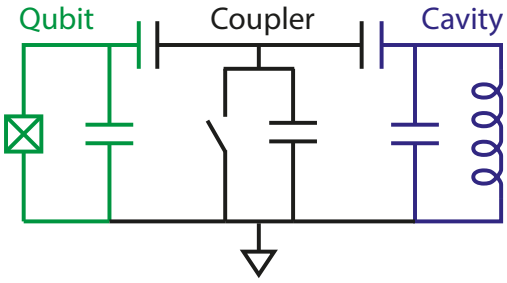

Figure 5.4: By placing a capacitive voltage divider between a qubit and a resonator the effective coupling can be changed. A digital switch in the circuit allows the coupling strength to be controlled.

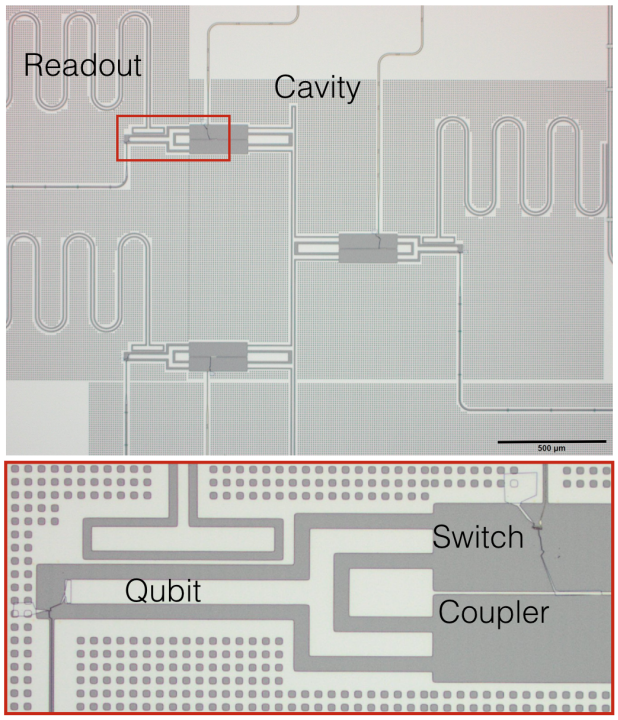

Figure 5.5: Three 'Y'-shaped gatemons are coupled to a common cavity through individual couplers. The qubits are coherently driven through the gate line.

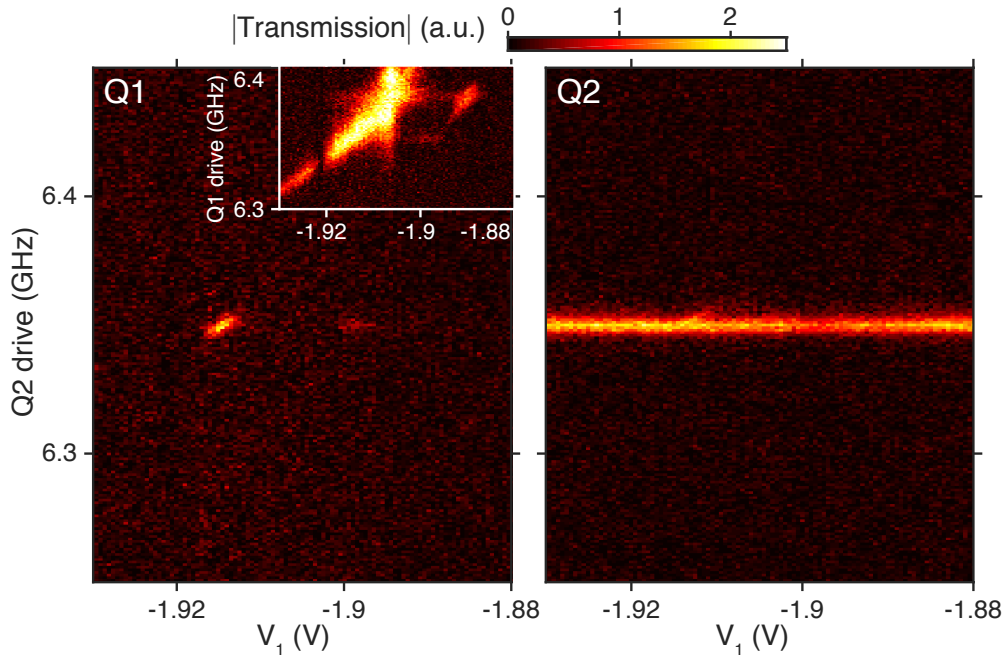

Figure 5.6: Simultaneous readout of Q1 and Q2 respectively as a function of Q1 gate voltage and Q2 drive frequency. Inset is the response of Q1 in the same gate voltage range but driving Q1 showing that the gate voltage modulates the frequency of Q1. The signal disappearing just below -1.92 V is a measurement artifact. An offset is subtracted from each column.

10^{-4} with the 'on' coupling strength simulated to be $\sim$20 MHz and a residual coupling in the off state being $\sim$2 kHz (Δ was assumed to be 0.5 GHz).

The data presented is from a sample where only two qubits and one tunable coupler are working due to low fabrication yield. The other coupler did not have a nanowire switch contacted, effectively ensuring that the coupler is on at all times. Even with the low yield we have enough to do proof of principle demonstrations by controlling the coupler for one qubit to the cavity while the other is always coupled. The cavity is designed to have a frequency of 6.75 GHz and the qubits are measured around 6.35 GHz ($\Delta \sim 0.4$ MHz). It is not possible to directly probe the cavity resonance frequency as there is no direct coupling from the feedline to the cavity.

We first investigate the system with the coupler turned off. To measure the residual coupling Q2 is parked at 6.35 GHz while Q1 is swept through as presented in Figure 5.6. The inset shows the frequency response of Q1 as a function of the gate voltage, V_1. A hole in the spectrum just below -1.92 V is a measurement artifact. We observe that the frequency is swept through the frequency of Q2 at 6.35 GHz. To probe the coupling we drive Q2 and measure the response of both qubits simultaneously. The residual coupling for qubits in this sample is expected to be of the order 0.25 MHz as only one coupler could be turned off. We do observe a response in Q1 as the qubits are on resonance consistent with a weak coupling between the qubits. A quantitative measurement of the coupling strength is not possible due to weak readout signal.

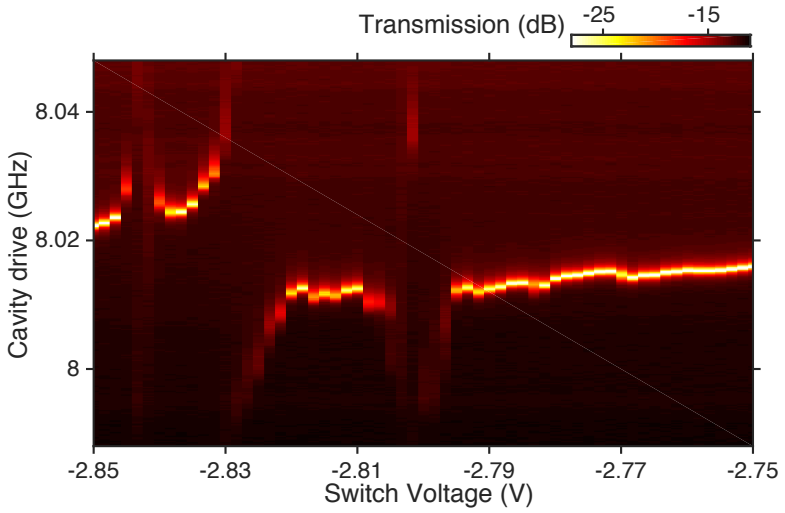

Figure 5.7: Vacuum Rabi splitting between the coupler and readout resonator of Q2 as a function of Cavity Drive and Switch Voltage.

Next we move to the strong coupling regime with the coupler turned on. However, when opening the switch the coupling does not turn on as expected. What we observe instead, is a dispersive shift on the qubit frequency due to the coupler. In Figure 5.7 the resonance frequency of the readout resonator is shown as the nanowire of the coupler is being pinched off. We observe an avoided crossing, which can be understood as a vacuum-Rabi splitting of the coupler-cavity system. When the nanowire is pinched off it moves through an intermediate regime where the coupler behaves as a qubit. The charging energy of the coupler is simulated to $E_C/h = 220$ MHz, very similar to a qubit. Going from one regime to the other will influence the qubit states, introducing errors. For this scheme to work, we need a switch that is digital, that is 'on' or 'off' with no intermediate regime.

Chapter 6

Conclusions and Outlook

In this thesis, semiconductor-nanowire-based superconducting qubits, gatemons, have been presented. The semiconductor-nanowire Josephson junction exchanges dissipative current control with nondissipating voltage control. Such a gatemon placed in a cQED architecture achieves strong cavity-qubit coupling exhibited by the vacuum-Rabi splitting in the resonant regime. In the dispersive regime, the spectrum of a gatemon qubit is mapped as a function of nanowire gate voltage. We observe an aperiodic energy spectrum consistent with the expected modulation of the semiconductor nanowire. With microwaves full coherent control of a single qubit is demonstrated. Fast control of the gate voltage allows coherent pulsing of the gatemon energy on a nanosecond time scale. Employing fast control, a coherent two-qubit coupling is demonstrated.

While first generation of gatemons has lifetimes of $\sim$0.8 μs, after only one round of optimization in fabrication and sample shielding the following samples show lifetimes up to 5 μs. Future research will focus on further extending the lifetimes of gatemons. By carefully optimizing the full fabrication process and sample shielding we hope to reach state of the art transmon lifetimes in gatemons.

It was furthermore investigated whether nanowire Josephson junctions can be used to create tunable coupling.. It was demonstrated that it is possible to modulate the frequency of a resonator. By coupling qubits to a tunable cavity it should be possible to tune the coupling between qubits. Implementing a tunable cavity with more qubits opens the possibility for all-to-all controlled qubit-qubit couplings. The results presented in this thesis strongly encourage further investigation into tunable cavities.

A different approach to tunable couplings between qubits was investigated. It relies on nanowire Josephson junctions acting as switches to effectively tune coupling capacitances. Couplings between qubits are indeed strongly suppressed when the coupler is turned off. However, we observe a vacuum-Rabi splitting as the coupler comes into resonance with the nearby readout resonator. From this we conclude that the coupler has to go through a regime where it acts as a qubit. As a qubit it interacts strongly with the system introducing errors.

In total, the gatemon poses a new potential qubit for quantum information processing that avoids large control currents. The results presented in this thesis encourage further

research in scalability and qubit performance as well as novel possibilities exploiting hybrid superconductor-semiconductor systems.

Appendix A: Fabrication

Detailed fabrication notes for samples measured in this thesis. Metal evaporation and *in situ* argon milling is done in an AJA International metal evaporation system. E-beam lithography is performed in a 100 kV Elionix electron beam lithography system. Optical lithography is performed with an Heidelberg μPG101 LED writer

Samples for Sections 4.1-4.4

Al film deposition

- Silicon substrate with thermal oxide cleaned in acetone and IPA
- Metal deposition: 1 min Ar mill, 75 nm Al

Gold alignment marks

- Resist spin: A4, 4000 rpm, 45 s, bake at 185°C for 4 min
- E-beam exposure: dose 1200 μC/cm^2
- Development: 60 s MIBK:IPA 1:3, 10 s IPA, O_2 plasma ash
- Metal deposition: 10 nm Ti, 40 nm Au
- Lift off: Acetone

Al film wet etching

- Resist spin: A4, 4000 rpm, 45 s, bake at 185°C for 4 min
- E-beam exposure: dose 1200 μC/cm^2
- Development: 60 s MIBK:IPA 1:3, 10 s IPA, O_2 plasma ash
- Etch: 25 s Transene Type D at 54°C, 30 s DI water, 10 s IPA
- Resist strip: Acetone

Nanowire deposition

- Resist spin: A4, 4000 rpm, 45 s, bake at 185°C for 4 min
- E-beam exposure: dose 1200 μC/cm^2
- Development: 60 s MIBK:IPA 1:3, 10 s IPA, O_2 plasma ash
- Nanowire dry deposition
- Resist strip: Acetone

Gold alignment marks for nanowire

- Resist spin: A4, 4000 rpm, 45 s, bake at 185°C for 4 min
- E-beam exposure: dose 1200 μC/cm^2
- Development: 60 s MIBK:IPA 1:3, 10 s IPA, O_2 plasma ash
- Metal deposition: 5 nm Ti, 35 nm Au
- Lift off: Acetone

Nanowire wet etch

- Resist spin: A4, 4000 rpm, 45 s, bake at 185°C for 4 min
- E-beam exposure: dose 1200 μC/cm^2
- Development: 60 s MIBK:IPA 1:3, 10 s IPA, O_2 plasma ash
- Etch: 12 s Transene Type D at 50°C, 30 s DI water, 10 s IPA
- Resist strip: Acetone

Nanowire contacts and side gate

- Resist spin: EL9, 4000 rpm, 45 s, bake at 185°C for 1 min
- Resist spin: A4, 4000 rpm, 45 s, bake at 185°C for 4 min
- E-beam exposure: dose 1200 μC/cm^2
- Development: 60 s MIBK:IPA 1:3, 10 s IPA, O_2 plasma ash
- Metal deposition: 3 min Ar mill, 1 nm Ti, 150 nm Al
- Resist strip: Acetone

Sample for Section 4.5

Al film deposition

- Silicon substrate with no thermal oxide cleaned in acetone and IPA
- Metal deposition: 1 min Ar mill, 75 nm Al

Gold alignment marks

- Resist spin: A4, 4000 rpm, 45 s, bake at 185°C for 3 min
- E-beam exposure: dose 1200 μC/cm^2
- Development: 60 s MIBK:IPA 1:3, 10 s IPA, O_2 plasma ash
- Metal deposition: 5 nm Ti, 45 nm Au
- Lift off: Acetone

Al film wet etching

- Resist spin: EL9, 4000 rpm, 45 s, bake at 185°C for 3 min
- Resist spin: CSAR4, 4000 rpm, 45 s, bake at 185°C for 3 min
- E-beam exposure: dose 450 μC/cm^2
- Development: 60 s O-xylene, 120 s MIBK:IPA 1:3, 15 s IPA, O_2 plasma ash
- Etch: 50 s Transene Type D at 53°C, 30 s DI water, 15 s IPA (longer etch time due to contaminated/old etch bottle)
- Resist strip: Acetone

Crossover oxide

- Resist spin: EL13, 4000 rpm, 45 s, bake at 185°C for 3 min
- Resist spin: CSAR4, 4000 rpm, 45 s, bake at 185°C for 3 min
- E-beam exposure: dose 450 μC/cm^2
- Development: 60 s O-xylene, 120 s MIBK:IPA 1:3, 15 s IPA, O_2 plasma ash
- Oxide deposition: 250 nm SiO_2
- Lift off: Acetone

Crossover metal

- Resist spin: EL13, 4000 rpm, 45 s, bake at 185°C for 3 min
- Resist spin: CSAR4, 4000 rpm, 45 s, bake at 185°C for 3 min
- E-beam exposure: dose 450 μC/cm^2
- Development: 60 s O-xylene, 120 s MIBK:IPA 1:3, 15 s IPA, O_2 plasma ash
- Metal deposition: 3 min Ar mill, 300 nm Al
- Lift off: Acetone

Nanowire deposition

- Resist spin: EL9, 4000 rpm, 45 s, bake at 185°C for 3 min
- E-beam exposure: dose 450 μC/cm^2
- Development: 60 s MIBK:IPA 1:3, 10 s IPA, O_2 plasma ash
- Nanowire dry deposition
- Resist strip: Acetone

Nanowire wet etch

- Resist spin: A4, 4000 rpm, 45 s, bake at 185°C for 4 min
- E-beam exposure: dose 1200 μC/cm^2
- Development: 60 s MIBK:IPA 1:3, 10 s IPA, O_2 plasma ash
- Etch: 12 s Transene Type D at 50°C, 30 s DI water, 10 s IPA
- Resist strip: Acetone

Gold alignment marks for nanowire

- Resist spin: A4, 4000 rpm, 45 s, bake at 185°C for 3 min
- E-beam exposure: dose 1200 μC/cm^2
- Development: 60 s MIBK:IPA 1:3, 10 s IPA, O_2 plasma ash
- Metal deposition: 5 nm Ti, 45 nm Au
- Lift off: Acetone

Nanowire contacts and side gate

- Resist spin: EL9, 4000 rpm, 45 s, bake at 185°C for 1 min
- Resist spin: A4, 4000 rpm, 45 s, bake at 185°C for 4 min
- E-beam exposure: dose 1200 μC/cm^2
- Development: 60 s MIBK:IPA 1:3, 10 s IPA, O_2 plasma ash
- Metal deposition: 5.5 min Ar mill, 1 nm Ti, 150 nm Al
- Resist strip: Acetone

Al film wet etching

- Resist spin: EL9, 4000 rpm, 45 s, bake at 185°C for 3 min
- Resist spin: CSAR4, 4000 rpm, 45 s, bake at 185°C for 3 min
- E-beam exposure: dose 450 μC/cm^2
- Development: 60 s O-xylene, 120 s MIBK:IPA 1:3, 15 s IPA, O_2 plasma ash
- Etch: 20 s Transene Type D at 53°C, 30 s DI water, 15 s IPA
- Resist strip: Acetone

Sample for Section 5.2

Al film deposition

- Silicon substrate with no thermal oxide cleaned in acetone and IPA
- Metal deposition: 1 min Ar mill, 100 nm Al

Gold alignment marks

- Resist spin: EL9, 4000 rpm, 45 s, bake at 185°C for 3 min
- Resist spin: CSAR9, 4000 rpm, 45 s, bake at 185°C for 3 min
- E-beam exposure: dose 450 μC/cm^2
- Development: 60 s O-xylene, 75 s MIBK:IPA 1:3, 15 s IPA, O_2 plasma ash
- Oxide deposition: 5 nm Ti, 95 nm Au
- Lift off: Acetone

Al film wet etching

- Resist spin: AZ1505, 4000 rpm, 45 s, bake at 115°C for 1 min
- UV exposure: dose 17 ms
- Development: 30 s MIBK:IPA 1:3, 30 s DI water, O_2 plasma ash
- Etch: 90 s Transene Type D at 50°C, 30 s DI water, 10 s IPA
- Resist strip: NMP, acetone

Nanowire deposition

- Resist spin: EL9, 4000 rpm, 45 s, bake at 185°C for 3 min
- E-beam exposure: dose 450 $\mu C/cm^2$
- Development: 60 s MIBK:IPA 1:3, 10 s IPA, O_2 plasma ash
- Nanowire dry deposition
- Resist strip: Acetone

Nanowire wet etch

- Resist spin: A4, 4000 rpm, 45 s, bake at 185°C for 4 min
- E-beam exposure: dose 1200 $\mu C/cm^2$
- Development: 60 s MIBK:IPA 1:3, 10 s IPA, O_2 plasma ash
- Etch: 12 s Transene Type D at 50°C, 30 s DI water, 10 s IPA
- Resist strip: Acetone

Nanowire contacts

- Resist spin: EL9, 4000 rpm, 45 s, bake at 185°C for 3 min
- Resist spin: CSAR9, 4000 rpm, 45 s, bake at 185°C for 3 min
- E-beam exposure: dose 450 $\mu C/cm^2$
- Development: 60 s O-xylene, 75 s MIBK:IPA 1:3, 10 s IPA, O_2 plasma ash
- Metal deposition: 4.5 min Ar mill, 1 nm Ti, 150 nm Al
- Resist strip: Acetone

ALD layer for top gate

- Resist spin: EL13, 4000 rpm, 45 s, bake at 185°C for 3 min
- Resist spin: CSAR9, 4000 rpm, 45 s, bake at 185°C for 3 min
- E-beam exposure: dose 450 μC/cm^2
- Development: 60 s O-xylene, 75 s MIBK:IPA 1:3, 10 s IPA, O_2 plasma ash
- ALD: ZrO_2 175 cycles at 100°C
- Resist strip: NMP

Nanowire top gate

- Resist spin: EL9, 4000 rpm, 45 s, bake at 185°C for 3 min
- Resist spin: CSAR9, 4000 rpm, 45 s, bake at 185°C for 3 min
- E-beam exposure: dose 450 μC/cm^2
- Development: 60 s O-xylene, 75 s MIBK:IPA 1:3, 10 s IPA, O_2 plasma ash
- Metal deposition: 1 nm Ti, 150 nm Al
- Resist strip: Acetone

Sample for Section 5.3

Al film deposition

- Silicon substrate with no thermal oxide cleaned in acetone and IPA
- Metal deposition: 15 s light Ar mill, 100 nm Al

Al film dry etching

- Resist spin: AZ1505, 4000 rpm, 45 s, bake at 115°C for 1.5 min
- UV exposure: dose 20 ms
- Development: 60 s AZ developer, 30 s DI water, 30 s DI water, O_2 plasma ash
- Reactive Ion etching: Cl_2 aluminum oxide etch 15 s, Cl_2/HBr aluminum etch 12 s
- Resist strip: NMP, acetone

Gold alignment marks

- Resist spin: AZ1505, 4000 rpm, 45 s, bake at 115°C for 1.5 min
- UV exposure: dose 20ms
- Development: 60 s AZ developer, 30 s DI water, 30 s DI water, O_2 plasma ash
- Metal deposition: 4 nm Ti, 41 nm Au
- Resist strip: NMP, acetone

Crossover oxide

- Resist spin: EL9, 4000 rpm, 45 s, bake at 185°C for 1 min
- Resist spin: CSAR9, 4000 rpm, 45 s, bake at 185°C for 3 min
- E-beam exposure: dose 450 $\mu C/cm^2$
- Development: 60 s O-xylene, 75 s MIBK:IPA 1:3, 15 s IPA, O_2 plasma ash
- Oxide deposition: 3.5 min Ar mill, 200 nm SiO_2
- Lift off: Acetone

Crossover metal

- Resist spin: EL9, 4000 rpm, 45 s, bake at 185°C for 1 min
- Resist spin: EL9, 4000 rpm, 45 s, bake at 185°C for 1 min
- Resist spin: CSAR9, 4000 rpm, 45 s, bake at 185°C for 3 min
- E-beam exposure: dose 450 $\mu C/cm^2$
- Development: 60 s O-xylene, 75 s MIBK:IPA 1:3, 15 s IPA, O_2 plasma ash
- Metal deposition:
- Lift off: Acetone

Gold alignment marks for nanowires

- Resist spin: EL9, 4000 rpm, 45 s, bake at 185°C for 1 min
- Resist spin: CSAR9, 4000 rpm, 45 s, bake at 185°C for 3 min
- E-beam exposure: dose 600 $\mu C/cm^2$
- Development: 60 s O-xylene, 75 s MIBK:IPA 1:3, 10 s IPA, O_2 plasma ash
- Metal deposition: 3 nm Ti, 42 nm Au
- Resist strip: NMP, acetone

Nanowire deposition

- Resist spin: EL9, 4000 rpm, 45 s, bake at 185°C for 3 min
- E-beam exposure: dose 600 μC/cm^2
- Development: 75 s MIBK:IPA 1:3, 10 s IPA, O_2 plasma ash
- Nanowire dry deposition
- Resist strip: Acetone

Nanowire wet etch

- Resist spin: A4, 4000 rpm, 45 s, bake at 185°C for 4 min
- E-beam exposure: dose 1200 μC/cm^2
- Development: 60 s MIBK:IPA 1:3, 10 s IPA, O_2 plasma ash
- Etch: 12 s Transene Type D at 50°C, 30 s DI water, 10 s IPA
- Resist strip: Acetone

Gold alignment marks for nanowire

- Resist spin: A4, 4000 rpm, 45 s, bake at 185°C for 3 min
- E-beam exposure: dose 1200 μC/cm^2
- Development: 60 s MIBK:IPA 1:3, 10 s IPA, O_2 plasma ash
- Metal deposition: 5 nm Ti, 45 nm Au
- Lift off: Acetone

Nanowire contacts and side gate for qubits

- Resist spin: EL9, 4000 rpm, 45 s, bake at 185°C for 1 min
- Resist spin: A4, 4000 rpm, 45 s, bake at 185°C for 4 min
- E-beam exposure: dose 1200 μC/cm^2
- Development: 60 s MIBK:IPA 1:3, 10 s IPA, O_2 plasma ash
- Metal deposition: 4.5 min Ar mill, 1 nm Ti, 150 nm Al
- Resist strip: Acetone

ALD layer for top gate for couplers

- Resist spin: EL13, 4000 rpm, 45 s, bake at 185°C for 3 min
- Resist spin: CSAR9, 4000 rpm, 45 s, bake at 185°C for 3 min
- E-beam exposure: dose 450 μC/cm^2
- Development: 60 s O-xylene, 75 s MIBK:IPA 1:3, 10 s IPA, O_2 plasma ash
- ALD: ZrO_2 175 cycles at 100°C
- Resist strip: NMP

Nanowire top gate for couplers

- Resist spin: EL9, 4000 rpm, 45 s, bake at 185°C for 3 min
- Resist spin: CSAR9, 4000 rpm, 45 s, bake at 185°C for 3 min
- E-beam exposure: dose 450 μC/cm^2
- Development: 60 s O-xylene, 75 s MIBK:IPA 1:3, 10 s IPA, O_2 plasma ash
- Metal deposition: 1 nm Ti, 150 nm Al
- Resist strip: Acetone

Bibliography

[1] G. E. Moore. "Cramming more components onto integrated circuits". Electronics (1965).

[2] A. M. Turing. "On Computable Numbers, with an Application to the Entscheidungsproblem". *Proceedings of the London Mathematical Society* **s2-42**, 230–265 (1937).

[3] R. P. Feynman. "Simulating physics with computers". *International Journal of Theoretical Physics* **21**, 467–488 (1982).

[4] D. Deutsch. "Quantum Theory, the Church-Turing Principle and the Universal Quantum Computer". In *Proceedings of the Royal Society A: Mathematical, Physical and Engineering Sciences*, 97–117 (1985).

[5] P. W. Shor. "Algorithms for Quantum Computation: Discrete Logarithms and Factoring ". In *Proceedings 35th Annual Symposium on Foundations of Computer Science*, 124–134 (IEEE, 1994).

[6] L. K. Grover. "A fast quantum mechanical algorithm for database search". In *the twenty-eighth annual ACM symposium*, 212–219 (ACM Press, New York, New York, USA, 1996).

[7] S. Lloyd. "Universal Quantum Simulators". *Science* **273**, 1073–1078 (1996).

[8] D. P. DiVincenzo. "The physical implementation of quantum computation". *Fortschritte Der Physik-Progress of Physics* **48**, 771–783 (2000).

[9] T. P. Harty, D. T. C. Allcock, C. J. Ballance, L. Guidoni, H. A. Janacek, N. M. Linke, D. N. Stacey & D. M. Lucas. "High-Fidelity Preparation, Gates, Memory, and Readout of a Trapped-Ion Quantum Bit". *Physical Review Letters* **113**, 220501 (2014).

[10] T. Monz, D. Nigg, E. A. Martinez, M. F. Brandl, P. Schindler, R. Rines, S. X. Wang, I. L. Chuang & R. Blatt. "Realization of a scalable Shor algorithm". *Science* **351**, 1068–1070 (2016).

[11] V. Mourik, K. Zuo, S. M. Frolov, S. R. Plissard, E. P. A. M. Bakkers & L. P. Kouwenhoven. "Signatures of Majorana Fermions in Hybrid Superconductor-Semiconductor Nanowire Devices". *Science* **336**, 1003–1007 (2012).

[12] S. M. Albrecht, A. P. Higginbotham, M. Madsen, F. Kuemmeth, T. S. Jespersen, J. Nygård, P. Krogstrup & C. M. Marcus. "Exponential protection of zero modes in Majorana islands". *Nature* **531**, 206–209 (2016).

[13] R. J. Schoelkopf & S. M. Girvin. "Wiring up quantum systems." *Nature* **451**, 664–669 (2008).

[14] F. Yan, S. Gustavsson, A. Kamal, J. Birenbaum, A. P. Sears, D. Hover, D. Rosenberg, G. Samach, T. J. Gudmundsen, J. L. Yoder, T. P. Orlando, J. Clarke, A. J. Kerman & W. D. Oliver. "The Flux Qubit Revisited to Enhance Coherence and Reproducibility". *arXiv.org* 1508.06299 (2015).

[15] N. Ofek, A. Petrenko, R. Heeres, P. Reinhold, Z. Leghtas, B. Vlastakis, Y. Liu, L. Frunzio, S. M. Girvin, L. Jiang, M. Mirrahimi, M. H. Devoret & R. J. Schoelkopf. "Extending the lifetime of a quantum bit with error correction in superconducting circuits". *Nature* 1–5 (2016).

[16] J. Koch, T. Yu, J. Gambetta, A. Houck, D. Schuster, J. Majer, A. Blais, M. Devoret, S. Girvin & R. Schoelkopf. "Charge-insensitive qubit design derived from the Cooper pair box". *Physical Review A* **76**, 042319 (2007).

[17] J. Schreier, A. Houck, J. Koch, D. Schuster, B. Johnson, J. Chow, J. Gambetta, J. Majer, L. Frunzio, M. Devoret, S. Girvin & R. Schoelkopf. "Suppressing charge noise decoherence in superconducting charge qubits". *Physical Review B* **77**, 180502 (2008).

[18] R. Barends, J. Kelly, A. Megrant, D. Sank, E. Jeffrey, Y. Chen, Y. Yin, B. Chiaro, J. Mutus, C. Neill, P. O'Malley, P. Roushan, J. Wenner, T. C. White, A. N. Cleland & J. M. Martinis. "Coherent Josephson qubit suitable for scalable quantum integrated circuits." *Physical Review Letters* **111**, 080502 (2013).

[19] A. D. Córcoles, E. Magesan, S. J. Srinivasan, A. W. Cross, M. Steffen, J. M. Gambetta & J. M. Chow. "Demonstration of a quantum error detection code using a square lattice of four superconducting qubits." *Nature Communications* **6**, 6979 (2015).

[20] P. W. Shor. "Scheme for reducing decoherence in quantum computer memory". *Physical Review A* **52**, R2493–R2496 (1995).

[21] M. A. Nielsen & I. L. Chuang. *Quantum Computation and Quantum Information.* 10th Anniversary Edition (Cambridge University Press, Cambridge, 2009).

[22] B. M. Terhal. "Quantum error correction for quantum memories". *Reviews of Modern Physics* **87**, 307–346 (2015).

[23] R. Barends, J. Kelly, A. Megrant, A. Veitia, D. Sank, E. Jeffrey, T. C. White, J. Mutus, A. G. Fowler, B. Campbell, Y. Chen, Z. Chen, B. Chiaro, A. Dunsworth, C. Neill, P. O'Malley, P. Roushan, A. Vainsencher, J. Wenner, A. N. korotkov, A. N.

Cleland & J. M. Martinis. "Superconducting quantum circuits at the surface code threshold for fault tolerance". *Nature* **508**, 500–503 (2014).

[24] A. G. Fowler, M. Mariantoni, J. M. Martinis & A. N. Cleland. "Surface codes: Towards practical large-scale quantum computation". *Physical Review A* **86**, 032324 (2012).

[25] J. Kelly, R. Barends, A. G. Fowler, A. Megrant, E. Jeffrey, T. C. White, D. Sank, J. Y. Mutus, B. Campbell, Y. Chen, Z. Chen, B. Chiaro, A. Dunsworth, I. C. Hoi, C. Neill, P. J. J. O'Malley, C. Quintana, P. Roushan, A. Vainsencher, J. Wenner, A. N. Cleland & J. M. Martinis. "State preservation by repetitive error detection in a superconducting quantum circuit". *Nature* **519**, 66–69 (2015).

[26] M. Takita, A. D. Córcoles, E. Magesan, B. Abdo, M. Brink, A. Cross, J. M. Chow & J. M. Gambetta. "Demonstration of weight-four parity measurements in the surface code architecture". *arXiv.org* 1605.01351 (2016).

[27] M. Reiher, N. Wiebe, K. M. Svore, D. Wecker & M. Troyer. "Elucidating Reaction Mechanisms on Quantum Computers". *arXiv.org* 1605.03590 (2016).

[28] G. de Lange, B. van Heck, A. Bruno, D. J. van Woerkom, A. Geresdi, S. R. Plissard, E. P. A. M. Bakkers, A. R. Akhmerov & L. DiCarlo. "Realization of Microwave Quantum Circuits Using Hybrid Superconducting-Semiconducting Nanowire Josephson Elements". *Physical Review Letters* **115**, 127002 (2015).

[29] T. W. Larsen, K. D. Petersson, F. Kuemmeth, T. S. Jespersen, P. Krogstrup, J. Nygård & C. M. Marcus. "Semiconductor-Nanowire-Based Superconducting Qubit". *Physical Review Letters* **115**, 127001 (2015).

[30] S. J. Srinivasan, A. J. Hoffman, J. M. Gambetta & A. A. Houck. "Tunable Coupling in Circuit Quantum Electrodynamics Using a Superconducting Charge Qubit with a V-Shaped Energy Level Diagram". *Physical Review Letters* **106**, 083601 (2011).

[31] J. D. Whittaker, F. C. S. da Silva, M. S. Allman, F. Lecocq, K. Cicak, A. J. Sirois, J. D. Teufel, J. Aumentado & R. W. Simmonds. "Tunable-cavity QED with phase qubits". *Physical Review B* **90**, 024513 (2014).

[32] Y. Chen, C. Neill, P. Roushan, N. Leung, M. Fang, R. Barends, J. Kelly, B. Campbell, Z. Chen, B. Chiaro, A. Dunsworth, E. Jeffrey, A. Megrant, J. Y. Mutus, P. J. J. O'Malley, C. M. Quintana, D. Sank, A. Vainsencher, J. Wenner, T. C. White, M. R. Geller, A. N. Cleland & J. M. Martinis. "Qubit Architecture with High Coherence and Fast Tunable Coupling". *Physical Review Letters* **113**, 220502 (2014).

[33] D. C. McKay, S. Filipp, A. Mezzacapo, E. Magesan, J. M. Chow & J. M. Gambetta. "A universal gate for fixed-frequency qubits via a tunable bus". *arXiv.org* 1604.03076 (2016).

[34] P. Krogstrup, N. L. B. Ziino, W. Chang, S. M. Albrecht, M. H. Madsen, E. Johnson, J. Nygård, C. M. Marcus & T. S. Jespersen. "Epitaxy of semiconductor–superconductor nanowires". *Nature Materials* **14**, 400–406 (2015).

[35] W. Chang, S. M. Albrecht, T. S. Jespersen, F. Kuemmeth, P. Krogstrup, J. Nygård & C. M. Marcus. "Hard gap in epitaxial semiconductor–superconductor nanowires". *Nature Nanotechnology* **10**, 232–236 (2015).

[36] L. Casparis, T. W. Larsen, M. S. Olsen, F. Kuemmeth, P. Krogstrup, J. Nygård, K. D. Petersson & C. M. Marcus. "Gatemon Benchmarking and Two-Qubit Operations". *Physical Review Letters* **116**, 150505 (2016).

[37] A. Blais, R.-S. Huang, A. Wallraff, S. M. Girvin & R. J. Schoelkopf. "Cavity quantum electrodynamics for superconducting electrical circuits: An architecture for quantum computation". *Physical Review A* **69**, 062320 (2004).

[38] S. M. Girvin. "Circuit QED: Superconducting Qubits Coupled to Microwave Photons". *Oxford University Press* (2011).

[39] M. Tinkham. "Introduction to Superconductivity". Dover Publications (1996).

[40] B. D. Josephson. "Possible new effects in superconductive tunnelling". *Physics Letters* **1**, 251–253 (1962).

[41] S. Chuang, Q. Gao, R. Kapadia, A. C. Ford, J. Guo & A. Javey. "Ballistic InAs Nanowire Transistors". *Nano Letters* **13**, 555–558 (2013).

[42] M. Hell, M. Leijnse & K. Flensberg. *To be submitted.* (2016).

[43] C. Beenakker. "Universal limit of critical-current fluctuations in mesoscopic Josephson junctions". *Physical Review Letters* (1991).

[44] A. Kringhøj. *Readout and Control of Semiconductor Nanowire-Based Superconducting Qubits.* Master's thesis, University of Copenhagen (2016).

[45] R. J. Schoelkopf, A. A. Clerk, S. M. Girvin, K. W. Lehnert & M. H. Devoret. "Noise and measurement backaction in superconducting circuits: qubits as spectrometers of quantum noise". In *SPIE's First International Symposium on Fluctuations and Noise* (eds. L. B. Kish, F. Green, G. Iannaccone & J. R. Vig), 356 (SPIE, 2003).

[46] D. I. Schuster, A. A. Houck, J. A. Schreier, A. Wallraff, J. M. Gambetta, A. Blais, L. Frunzio, J. Majer, B. Johnson, M. H. Devoret, S. M. Girvin & R. J. Schoelkopf. "Resolving photon number states in a superconducting circuit". *Nature* **445**, 515–518 (2007).

[47] B. Vlastakis, G. Kirchmair, Z. Leghtas, S. E. Nigg, L. Frunzio, S. M. Girvin, M. Mirrahimi, M. H. Devoret & R. J. Schoelkopf. "Deterministically encoding quantum information using 100-photon Schrödinger cat states." *Science* **342**, 607–610 (2013).

[48] D. Ristè, C. C. Bultink, K. W. Lehnert & L. DiCarlo. "Feedback Control of a Solid-State Qubit Using High-Fidelity Projective Measurement". *Physical Review Letters* **109**, 240502 (2012).

[49] A. Houck, J. Schreier, B. Johnson, J. Chow, J. Koch, J. Gambetta, D. Schuster, L. Frunzio, M. Devoret, S. Girvin & R. Schoelkopf. "Controlling the Spontaneous Emission of a Superconducting Transmon Qubit". *Physical Review Letters* **101**, 080502 (2008).

[50] E. Jeffrey, D. Sank, J. Y. Mutus, T. C. White, J. Kelly, R. Barends, Y. Chen, Z. Chen, B. Chiaro, A. Dunsworth, A. Megrant, P. J. J. O'Malley, C. Neill, P. Roushan, A. Vainsencher, J. Wenner, A. N. Cleland & J. M. Martinis. "Fast Accurate State Measurement with Superconducting Qubits". *Physical Review Letters* **112**, 190504 (2014).

[51] A. Dewes, F. R. Ong, V. Schmitt, R. Lauro, N. Boulant, P. Bertet, D. Vion & D. Esteve. "Characterization of a Two-Transmon Processor with Individual Single-Shot Qubit Readout". *Physical Review Letters* **108**, 057002 (2012).

[52] J. Majer, J. M. Chow, J. M. Gambetta, J. Koch, B. R. Johnson, J. A. Schreier, L. Frunzio, D. I. Schuster, A. A. Houck, A. Wallraff, A. Blais, M. H. Devoret, S. M. Girvin & R. J. Schoelkopf. "Coupling superconducting qubits via a cavity bus". *Nature* **449**, 443–447 (2007).

[53] M. Reed. *Entanglement and Quantum Error Correction with Superconducting Qubits*. Ph.D. thesis, Yale University (2013).

[54] T. Tanamoto, K. Maruyama, Y.-x. Liu, X. Hu & F. Nori. "Efficient purification protocols using iSWAPgates in solid-state qubits". *Physical Review A* **78**, 062313 (2008).

[55] L. DiCarlo, J. M. Chow, J. M. Gambetta, L. S. Bishop, B. R. Johnson, D. I. Schuster, J. Majer, A. Blais, L. Frunzio, S. M. Girvin & R. J. Schoelkopf. "Demonstration of two-qubit algorithms with a superconducting quantum processor". *Nature* **460**, 240–244 (2009).

[56] J. Kelly, R. Barends, B. Campbell, Y. Chen, Z. Chen, B. Chiaro, A. Dunsworth, A. G. Fowler, I. C. Hoi, E. Jeffrey, A. Megrant, J. Mutus, C. Neill, P. J. J. O'Malley, C. Quintana, P. Roushan, D. Sank, A. Vainsencher, J. Wenner, T. C. White, A. N. Cleland & J. M. Martinis. "Optimal Quantum Control Using Randomized Benchmarking". *Physical Review Letters* **112**, 240504 (2014).

[57] W. Chang. *Superconducting Proximity Effect in InAs Nanowires*. Ph.D. thesis, Harvard University (2014).

[58] W. E. Shanks, D. L. Underwood & A. A. Houck. "A scanning transmon qubit for strong coupling circuit quantum electrodynamics". *Nature Communications* **4**, 1–6 (2013).

[59] A. Wallraff, D. I. Schuster, A. Blais, L. Frunzio, R.-S. Huang, J. Majer, S. Kumar, S. M. Girvin & R. J. Schoelkopf. "Strong coupling of a single photon to a superconducting qubit using circuit quantum electrodynamics." *Nature* **431**, 162–167 (2004).

[60] . Cywiński. "Dynamical-decoupling noise spectroscopy at an optimal working point of a qubit". *Physical Review A* **90**, 042307 (2014).

[61] L. DiCarlo, M. D. Reed, L. Sun, B. R. Johnson, J. M. Chow, J. M. Gambetta, L. Frunzio, S. M. Girvin, M. H. Devoret & R. J. Schoelkopf. "Preparation and measurement of three-qubit entanglement in a superconducting circuit". *Nature* **467**, 574–578 (2010).

[62] D. Ristè, C. C. Bultink, M. J. Tiggelman, R. N. Schouten, K. W. Lehnert & L. DiCarlo. "Millisecond charge-parity fluctuations and induced decoherence in a superconducting transmon qubit." *Nature Communications* **4**, 1913 (2013).